




Interplay between spin wave and magnetic vortex

Zhongchen Gao ^{1,*}, Feifei Wang ¹, Xiangyong Zhao,¹ Tao Wang,¹ Jingguo Hu,² and Peng Yan ³

¹Mathematics and Science College, Shanghai Normal University, Shanghai 200233, China

²School of Physical Science and Technology, Yangzhou University, Yangzhou 225002, China

³School of Physics and State Key Laboratory of Electronic Thin Films and Integrated Devices, University of Electronic Science and Technology of China, Chengdu 610054, China



(Received 5 December 2022; revised 4 April 2023; accepted 31 May 2023; published 13 June 2023)

The interplay between spin wave (SW) and magnetic vortex is studied. We find three types of magnon scatterings: skew scattering, symmetric side deflection, and back reflection, which associate with, respectively, magnetic topology, energy density distribution, and linear momentum transfer torque within the vortex. The vortex core exhibits two translational modes: the intrinsic circular mode and a coercive elliptical mode, which can be excited by the net and oscillating magnon spin-transfer torque effects of SWs. Lastly, we propose a vortex-based SW valve in which we obtain excellent valving performance and access arbitrary control of the phase shift via inhomogeneity modulation. The phase shift arises from the enlarged wavelength of the SW in inhomogeneous magnetization.

DOI: [10.1103/PhysRevB.107.214418](https://doi.org/10.1103/PhysRevB.107.214418)

I. INTRODUCTION

Spin waves (SWs) or magnons are fundamental collective excitations of the spin order [1–3] and have been considered ideal information carriers, taking advantage of their free-of-charge transport (hence low-energy dissipation) and orders-of-magnitude smaller wavelength compared with electromagnetic waves (hence downscale devices) [4,5]. The excitation, propagation, control, and detection of SWs have opened the field of magnonics [4–6]. On the other hand, a vortex represents the simplest pattern of domain configuration in a magnetic particle with in-plane curling magnetization around out-of-plane magnetization at the core [7,8]. Such a structure is topologically protected (commonly referred to as a magnetic soliton [9]) and characterized by the binary properties of chirality \mathbf{C} and polarity \mathbf{P} , each of which suggests an independent bit of information useful in future high-density memory storage and logic devices [10,11]. Study of the interplay between SW and vortex is interesting in two aspects: (i) SW and vortex structure together make up a highly nonlinear ferromagnetic system which provides an excellent platform to explore the rich physics in nonlinear science; (ii) it holds an intimate connection to technological development of both magnonic devices and vortex-based applications (notably, vortex-based SW excitation [12–15], transportation [16–18], and manipulation [19–22] as well as SW-involved vortex stability [23], reversal [24–28], and dynamics [29–31] have been given considerable attention) and finally facilitates the realization of a purely magnetic computing scheme [32,33].

Early studies on the magnon-vortex interaction mainly focused on SWs that belong to the eigenmodes of the magnetic

vortex. Specifically, there are the radial SW mode (with diametric nodes n) typically driven by an out-of-plane field and the azimuthal SW mode (with circular nodes m) typically excited by an in-plane field [34–41]. Relevant findings partly include those of Park *et al.* [30], who studied the interaction of the azimuthal mode with a vortex using time-resolved Kerr microscopy and found that the azimuthal mode can split into a doublet [22]. Such splitting later was analytically shown to be a result of dynamic hybridization of two regular azimuthal dipolar modes and a Goldstone-like gyrotropic mode [21]. By taking advantage of such splitting, Kammerer *et al.* [25] demonstrated experimentally the polarization-selective vortex core (VC) reversal with excitation of the azimuthal modes. On the other hand, based on micromagnetic simulation, Choi *et al.* [14] reported strong radiation of radial SWs through frequent reversal of the VC [42]. Wintz *et al.* [12] experimentally presented radial SWs with linear and nonreciprocal dispersion based on the gyrations in magnetic vortex pairs. Yoo *et al.* [24] further pointed out numerically that the radial SW eigenmodes can assist the VC switching. In some other research, Buess *et al.* [43] obtained direct observation of simultaneous excitations of radial and azimuthal SWs based on fast perturbation to overall vortex magnetization. Bauer *et al.* [27], through detailed micromagnetic studies, revealed the interference effect between the radial and azimuthal modes and a variety of nonlinear effects between the SWs and an initially gyrating core. Ruiz *et al.* [44], by means of time-resolved scanning Kerr microscopy imaging, discovered the curling nature of vortex states upon concurrent excitations of gyrotropic core dynamics, spiral SWs, and azimuthal and radial modes. Most recently, Wang *et al.* [45] suggested theoretically that the three-magnon confluence and splitting scattering of azimuthal SWs off the gyrating VC can generate a set of discrete and equally spaced spectral lines, hence a twisted magnon frequency comb.

*Corresponding author: gaozc0129@shnu.edu.cn

Despite the fruitful results achieved, the demand of long-distance travelling SWs for information transmission has been largely overlooked. Note that the radial and azimuthal SWs are commonly locally excited and confined within an isolated geometry (e.g., disk or dot). However, in magnonics, following the pace of CMOS technology, practical applications such as logic gates and memories need to be cascaded and form circuitry. Interconnects are key elements for any circuit. In the case of a magnonic circuit [46], these interconnects are often referred as SW buses, which can be manufactured based on magnetic thin-film nanostraps and undertaken to input, transport, and output magnonic signals. Naturally, the mutual effect between the SW current and subsequent magnonic devices becomes one major concern, as it determines how the signals are being processed. Thus, in this paper, particular attention is paid to the interaction of the vortex with unidirectional propagation of SWs, and we address three crucial problems: (1) How is the propagating SW being scattered? (2) How does the vortex react to the propagating SW? (3) How can we take advantage of this SW-vortex interaction? Particularly, for a vortex with stabilized winding number $+\frac{1}{2}$ or $-\frac{1}{2}$ (i.e., magnetization at the disk edge remains tangent, hence avoidance of surface magnetic charges), it could be viewed as half a Bloch-type skyrmion, as it covers half of the sphere in order parameter space $V = S^2$. The topologically nontrivial texture is thus promising to yield the magnon Hall effect as in skyrmions [47,48], which is of great interest and importance.

To reveal the interaction details, the underlying magnetization dynamics that is governed by the Landau-Lifshitz-Gilbert equation [49,50]:

$$\frac{\partial \mathbf{m}}{\partial t} = -\gamma \mathbf{m} \times \mathbf{h}_{\text{eff}} + \alpha \mathbf{m} \times \frac{\partial \mathbf{m}}{\partial t}, \quad (1)$$

(here, γ is the gyromagnetic ratio; \mathbf{h}_{eff} is the effective field that includes exchange interaction, dipole-dipole interaction, magnetocrystalline anisotropy, and Zeeman energy; and α is the Gilbert damping constant), is majorly numerically solved based on the MuMax³ code [51], whereas the related material parameters are adopted from permalloy (i.e., saturation magnetization $M_S = 8.6 \times 10^5 \text{ A m}^{-1}$, exchange stiffness $A = 1.3 \times 10^{-11} \text{ J m}^{-1}$), and the unit cell is chosen to be $4 \times 4 \times 5 \text{ nm}^3$ [52–54]. During the simulation, the Gilbert damping constant is set to be $\alpha = 0.001$ to ensure long-distance propagation of the SW beams [55].

This paper is organized as follows. In Sec. II, by tracing the trajectories of Gaussian beams of SWs through the magnetic texture, we reveal strong unilateral skew scattering and relatively weak symmetric side deflection of SWs. Based on the collective description of the interaction in the Lagrangian frame, the skew scattering is attributed to the topology-induced emergent field inside the core region. The symmetric side deflection, on the other hand, can be explained in terms of the local energy density distribution of the vortex. In Sec. III, from the fast Fourier transformations of the temporal variations of the VC position, we identify two modes of gyrations: a circular mode with fixed subgigahertz frequency and an ellipse-type mode with frequency the same as that of the propagating SW, which can be ascribed to the net and oscillating magnon spin-transfer torque (STT) effects, respec-

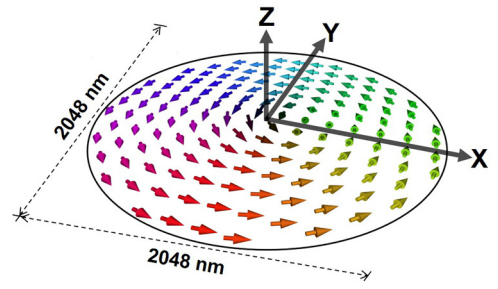


FIG. 1. Schematics of magnetic vortex in disk with chirality +1 and polarity -1.

tively. Section IV focuses on our proposal of a vortex-based SW valve (VSV), in which we achieve a tunable phase shift of SWs in addition to successful valving performance. The phase shift is found to arise from the enlarged wavelength of SWs in inhomogeneous magnetization and is determined to be a monotonically increasing function of the degree and dimensional span of the inhomogeneity of the contouring texture. Finally, a summary is given in Sec. V.

II. SCATTERINGS OF SW BY VORTEX

To start with, for the idealization and simplicity of modeling, we construct a single-layer disk with a diameter of 2048 nm, in which a standard vortex is initially stabilized with its core located at the center, see Fig. 1. The VC is spontaneously regularized to have an out-of-plane polarity instead of a singular point defect, hence the so-called Heisenberg vortex. To get a visualization on how SWs are being scattered by the vortex, a straightforward method is to trace their travelling trajectories, which can be done using Gaussian beams [55,56]. Here, we prepare multiple SW Gaussian beams at different vertical locations on the left side so that a thorough image of scattering can be obtained. Each beam is excited by applying a sinusoidal monochromatic microwave field $\mathbf{H}_{ac} = h_0 \sin(2\pi ft)\hat{z}$, where $f = 100 \text{ GHz}$ in a narrow rectangular region with its long side parallel to the wave front that is expected to move forward to the right (i.e., the $+x$ direction). The field amplitude h_0 has a Gaussian distribution $G(y) = \exp[-(y - y_0)^2 / (l\sigma)^2]$ along the y axis with its maximum set to be $h_{\text{max}} = 5 \text{ kOe}$. Here, l ($l = 128 \text{ nm}$) is the length of the excitation area, and σ^2 represents the variance of the Gaussian distribution centered around y_0 and is set to be $\frac{3}{4}$. Along the x axis, h_0 takes uniform values for a small window of width $w = 4 \text{ nm}$. To minimize the reflection of SWs from the disk edge, an absorbing boundary condition with a gradually increased damping constant from inside out is adopted for the outer-ring region, see the shadowed area in Fig. 2.

The tracked trajectories of the Gaussian beams have been highlighted using solid or dashed curves in Fig. 2. For a SW that passes through the central VC region, one clearly finds strong unilateral and sectorial scattering of the SW (see the black dashed curves that outline a spectrum of scatterings of a single Gaussian beam right across the center of the vortex), giving rise to the topological magnon Hall effect [48,57–59]. Notably, the direction of such scattering depends on the polarity of the VC, in which -1 ($+1$) gives rise to

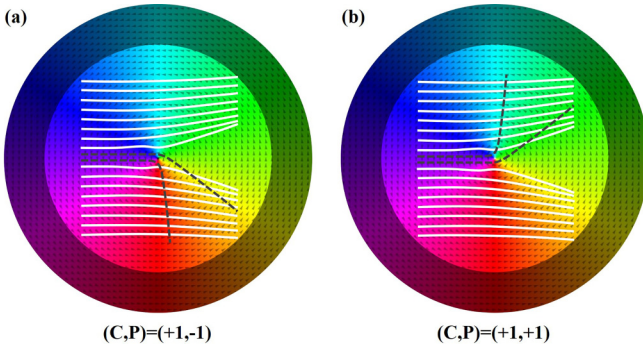


FIG. 2. Schematics of propagating spin waves (SWs) across (a) magnetic vortex with chirality +1 and polarity -1 [i.e., $(\mathbf{C}, \mathbf{P}) = (+1, -1)$] and (b) magnetic vortex with chirality +1 and polarity +1 [i.e., $(\mathbf{C}, \mathbf{P}) = (+1, +1)$] within disks (diameter and thickness: 2048 and 5 nm). The outer shadowed rings (width: 256 nm) are implemented with an absorbing boundary condition that gradually increases damping constant α as approaching the edge. SW Gaussian beams are excited on the left ~ 512 nm away from the core and are vertically evenly spaced with intervals of 64 nm. The solid white lines represent the propagating trajectories of the Gaussian beams through the vortex. The dashed black lines outline the sectorial scattering of a Gaussian beam across the center of the vortex.

downward (upward) scattering. On the other hand, for SWs that bypass the VC region, a relatively weak and symmetric side deflection is observed (see the white solid curves), and the beam trajectory depends on the impact parameter (i.e., the vertical shift from the VC). In general, those beams with smaller impact parameters are more strongly deflected. For large enough impact parameters, the deflection can be neglected. Through comparison between Figs. 2(a) and 2(b) of 180° x -axis rotation, one may further learn that the chirality affects neither the deflection outside the VC region nor the strong scattering inside the VC region. It is worth mentioning that, according to our observation, SWs with reduced frequency and amplitude lead to similar scattering behaviors.

To explain the strong sectorial scattering inside the VC, here, we follow the general dynamics of SWs and magnetic texture formulated in a Lagrangian frame [47]. By invoking the Euler-Lagrangian rule, employing minimal collective coordinates $\mathbf{X}_\mu = (X, Y)$ and neglecting texture corrections due to existence of local SW excitations, one can arrive at equations of motion in real space as

$$\dot{\mathbf{X}} \times B^0 \hat{\mathbf{z}} = -\rho \dot{\mathbf{x}} \times \vec{\mathfrak{B}}, \quad (2a)$$

$$m_{\text{sw}} \ddot{\mathbf{x}} + \dot{\mathbf{x}} \times b^0 \hat{\mathbf{z}} = \dot{\mathbf{X}} \times \vec{\mathfrak{B}}, \quad (2b)$$

where $m_{\text{sw}} = \frac{1}{2A}$ is the normalized effective mass of the excitation of the SW packet, ρ is the total SW intensity, \mathbf{X} and \mathbf{x} denote the central positions of the texture and the wave packet,

$$b^0 = \mathbf{m}_0 \cdot \left(\frac{\partial \mathbf{m}_0}{\partial x} \times \frac{\partial \mathbf{m}_0}{\partial y} \right) \quad (3)$$

is the effective magnetic field that corresponds to the magnetic topology of the texture,

$$B^0 = B_{xy}^0 = \int \mathbf{m}_0 \cdot \left(\frac{\partial \mathbf{m}_0}{\partial x} \times \frac{\partial \mathbf{m}_0}{\partial y} \right) dx dy = 4\pi \Omega \quad (4)$$

is the topological charge-associated magnetic field (here, Ω represents topological charge) that can in turn deflect the texture itself, and $\vec{\mathfrak{B}} = b^0 \hat{\mathbf{z}}$ formulates the total mutual magnetic field spanning both parameter spaces $\{\mathbf{x}_\mu, \mathbf{x}_i\}$ in which the texture and SW interact with each other (note that, as the Dzyaloshinskii-Moriya interaction is not involved in the vortex, contributions from the effective magnetic field b^D have been omitted). It is worth noting that the right-hand sides of Eqs. (2a) and (2b) indicate the magnonic STT exerted on the texture and the texture-induced motive force acting on the SW [60,61], respectively. According to Eq. (2b), obviously, a transverse velocity can be expected to arise for a SW traveling upon an inhomogeneous texture, which defines the skew scattering for SWs [47,48].

In Fig. 3, we show the two-dimensional (2D) topological charge density [$q = (1/4\pi) \mathbf{m} \cdot (\partial_x \mathbf{m} \times \partial_y \mathbf{m})$] distribution, which is in proportion to the effective magnetic field (or emergent field [62]) b^0 . Nonzero q does arise but within only the narrow VC region described in terms of the static polarization or m_z profile. The q (hence emergent field b^0) changes rapidly approaching the core center. However, the sign of q remains unchanged and depends definitively on the polarity, as expected. Due to the effective Lorentz force $F_j = v_i b_{ij}^0$, which SW packets would experience as they pass through the VC, the unilateral skew scattering corresponding to the Hall effect of magnons inside the core region naturally emerges.

It is worth mentioning that, as shown in Fig. 4, under the propagation of the SW beam right across the central VC region, the core itself is pulled to the left while undergoing upward (downward) movement for $P = -1$ ($P = +1$) due to the reaction force out of the skew scattering (recall that the VC can be deflected by its own topological field B^0), which is consistent with calculations based on Eq. (2a). Here, the core trajectories are traced in terms of the guiding center (X, Y) of the core, where $X = (\int x q dx dy) / (\int q dx dy)$, $Y = (\int y q dx dy) / (\int q dx dy)$ [63]. The oscillatory manner is believed to be attributed to the process of oscillating magnonic STT, as will be explained in Sec. III.

To understand the symmetric side deflection of SWs outside the VC, one may further examine the linearization of the Landau-Lifshitz-Gilbert equation under perturbation. In many cases, including the abovementioned Bloch-type skyrmion, the linearized LLG equation can be recast approximately into an effective Schrödinger equation as [64–66]

$$i\hbar(1 + i\alpha) \frac{\partial \Psi}{\partial t} = \left[\frac{1}{2\mu} (-i\hbar \nabla - \mathbb{A})^2 + \mathcal{V} \right] \Psi, \quad (5)$$

where $\Psi = m_\theta - im_\phi$ (m_θ, m_ϕ represent the SW excitations at polar and azimuthal angles of $\hat{\mathbf{m}}_0, \hat{\mathbf{m}}_0$, denoting static magnetization), $\mu = (\frac{\hbar}{\gamma}) \frac{1}{2A}$ is the effective SW mass, $\mathbb{A}(\mathbf{r})$ and $\mathcal{V}(\mathbf{r})$ are respectively the spatially varying effective vector and scalar potentials determined by the static magnetization profile. Considering the existence of the Gilbert damping constant on the left, hence no probability conservation, propagation of magnons in $\mathbb{A}(\mathbf{r})$ and $\mathcal{V}(\mathbf{r})$ is equivalent to electrons moving in certain vector and scalar potentials. The vector potential (note that the curl $\nabla \mathbb{A}(\mathbf{r})$ [57,66] gives rise to the effective magnetic field) and the corresponding effective magnetic field of the vortex, hence the skew scattering/topological Hall effect

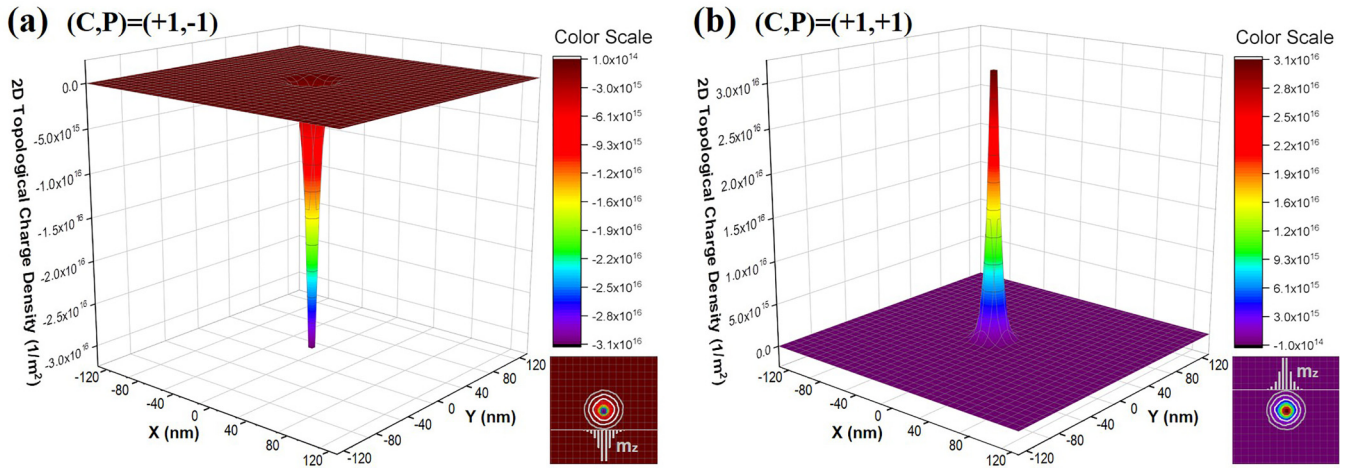


FIG. 3. Distribution of two-dimensional (2D) topological charge density (q) in (a) magnetic vortex with $(\mathbf{C}, \mathbf{P}) = (+1, -1)$ and (b) magnetic vortex with $(\mathbf{C}, \mathbf{P}) = (+1, +1)$. Insets at the lower right corners emphasize the small area of dominant q within radius of ~ 32 nm, which is comparative with the nonzero m_z profile of the core.

of SWs [57,67], have been reasonably discussed already. The scalar potential $\mathcal{V}(\mathbf{r})$ stemming from conventional texture inhomogeneity [64], however, has been disregarded so far.

In Fig. 5(a), we show the radial distribution of magnetic energy that is in proportion to the scalar potential [66] within a diameter of 256 nm in the VC with respect to the m_x and m_y profiles for the case $(\mathbf{C}, \mathbf{P}) = (+1, -1)$ [note that, for simplicity, we will focus on only the magnetic vortex with $(\mathbf{C}, \mathbf{P}) = (+1, -1)$ in the rest of this paper]. The total energy is mainly contributed by the exchange energy [see Fig. 5(b)], and finite energy density arises within only a limited area near the core with a dominant peak at the very center. Nevertheless, through comparison between the total energy density ($E_{\text{dens-total}}$) distribution and the q distribution in ln scale [see Fig. 5(c)], the former still turns out to be a lot more extensive in the radial dimension. As seen, q is highly confined within merely 64 nm in diameter. Such a difference between $E_{\text{dens-total}}$ and q in their active area could be responsible for the regionalization of the two scattering behaviors shown in Fig. 2.

By recalling that the partial derivative of the total energy density with respect to local magnetization corresponds to the effective field \mathbf{B}_{eff} (i.e., $\mathbf{B}_{\text{eff}} \propto \partial E_{\text{dens}} / \partial \mathbf{m}$), the internal field that is due to exchange and dipolar interactions has been determined over a circle diameter of 256 nm across the VC, as plotted in Fig. 5(d). As seen, component B_x (B_y) possesses the same symmetry as component m_x (m_y). However, B_y clearly exhibits enhanced inhomogeneity compared with m_y . The maxima of B_x and B_y both reach ~ 1 T. Interestingly, approaching the disk edge, B_x soon reduces to zero, whereas B_y can maintain its amplitude at a level of a few milliteslas at hundreds of nanometers (see the upper-left inset), which ensures a sizable deflection of SWs at locations in the far distance. By sweeping the $B_x(x)$ and $B_y(x)$ distributions around the z axis (recall the rotational symmetry of the vortex) while disregarding their signs, one can expect the formation of a single-peak potential by B_x and formation of a crater-shaped potential by B_y (see the lower-right inset). These potentials rationalize the symmetric side deflection outside the VC region.

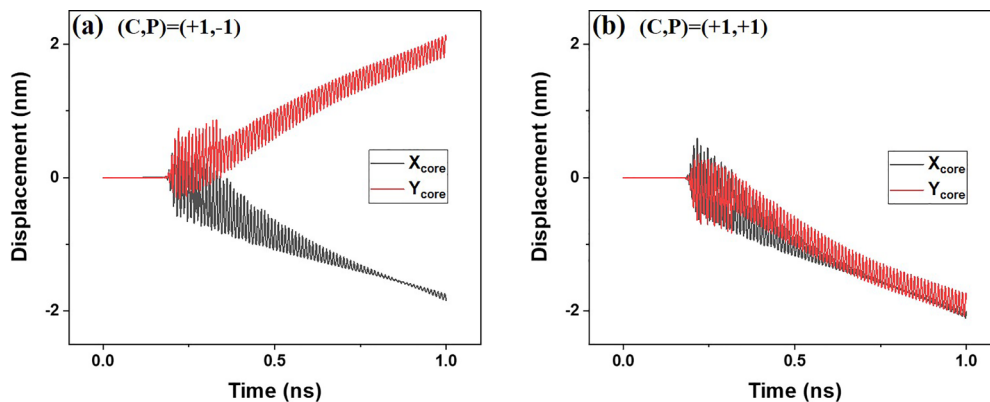


FIG. 4. Two-dimensional (2D) movements of the vortex core (VC) under propagation of spin-wave (SW) Gaussian beam through the central VC region in (a) magnetic vortex with $(\mathbf{C}, \mathbf{P}) = (+1, -1)$ and (b) magnetic vortex with $(\mathbf{C}, \mathbf{P}) = (+1, +1)$ within 1 ns.

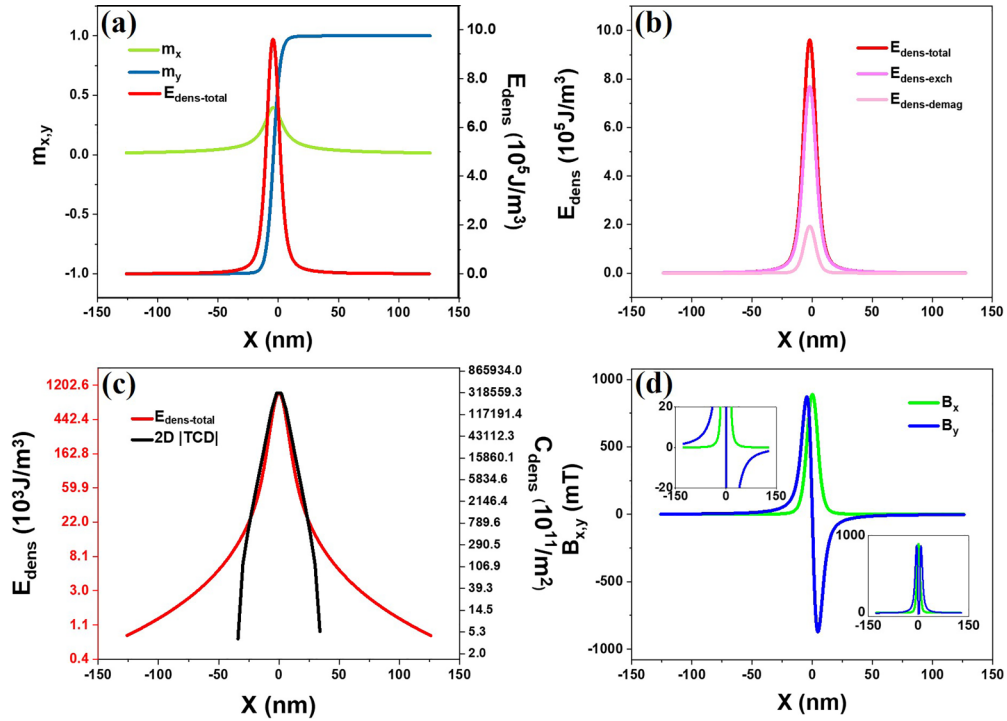


FIG. 5. Comparison between total energy density distribution and (a) magnetization distribution (here, $m_i = M_i/M_S$), (b) the components of exchange energy density and demagnetization energy density distributions, and (c) the absolute q distribution (C_{dens}) in ln scale over a circle diameter of 256 nm across the VC along the x axis, based on $(\mathbf{C}, \mathbf{P}) = (+1, -1)$. (d) The corresponding internal-field distributions of B_x and B_y over a circle diameter of 256 nm across the VC. Considering the rotational symmetry of the vortex, relevant characters are plotted with respect to the x axis only. The upper-left inset is a zoomed-in image of the plot. The lower-right inset depicts the absolute-field profiles of B_x and B_y .

As $\mathbf{B}_{\text{eff}} \propto \partial E_{\text{dens}} / \partial \mathbf{m}$, it is natural to predict that changing $E_{\text{dens-total}}$ and/or magnetization field \mathbf{m}_i shall lead to different scatterings of SWs. In Figs. 6(a) and 6(b), we obtain successful modulation on the scattering performance through simulations of spin systems with enlarged size or modified geometry. By repeating the Gaussian beam simulations, the beam trajectories have been traced using solid black lines, in contrast to the original trajectories (see the dashed red lines) reproduced from Fig. 2(a). Misalignments of the trajectories are clearly seen. More precisely, in the present two cases, SWs all become less deflected. Thus, to get stronger deflections, one may try out spin systems with reduced size.

III. DRIVEN TRANSLATIONAL MODES OF VC

In this section, we focus on the reciprocal dynamics of Sec. II—the driven motion of the VC by propagating SWs, which represents the other type of spin excitation (namely, translational or gyrotropic modes) existing in a magnetic vortex system [30,40,68]. The upper-left (lower-left) movement displayed in Fig. 4(a) [Fig. 4(b)] only reflects the initial displacement of the core under a narrow Gaussian beam. Patterned modes of motion when being immersed in laterally uniform pumping of SWs, however, remain unknown. To crack the problem, herein, we generate plane waves on the left with sufficiently larger width than the size of the VC. In

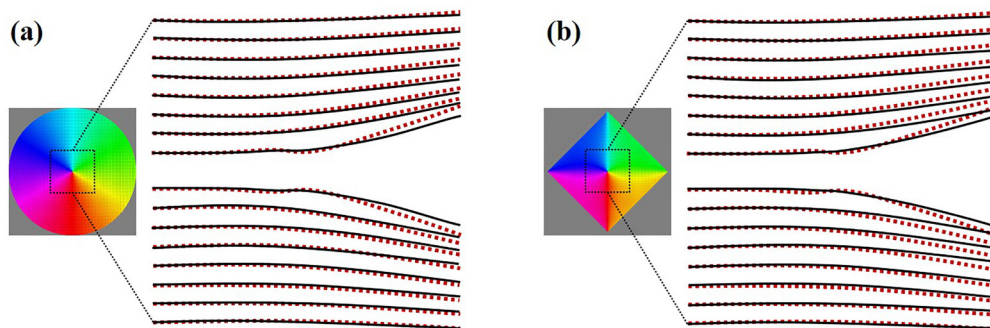


FIG. 6. Out-of-core trajectories (see the black solid lines) of Gaussian beams by (a) magnetic vortex within a disk of diameter 3072 nm and (b) magnetic vortex within a square plate with edge length 2048 nm. The dashed red lines mark the trajectories of out-of-core side deflections by the original vortex within a disk of diameter 2048 nm.

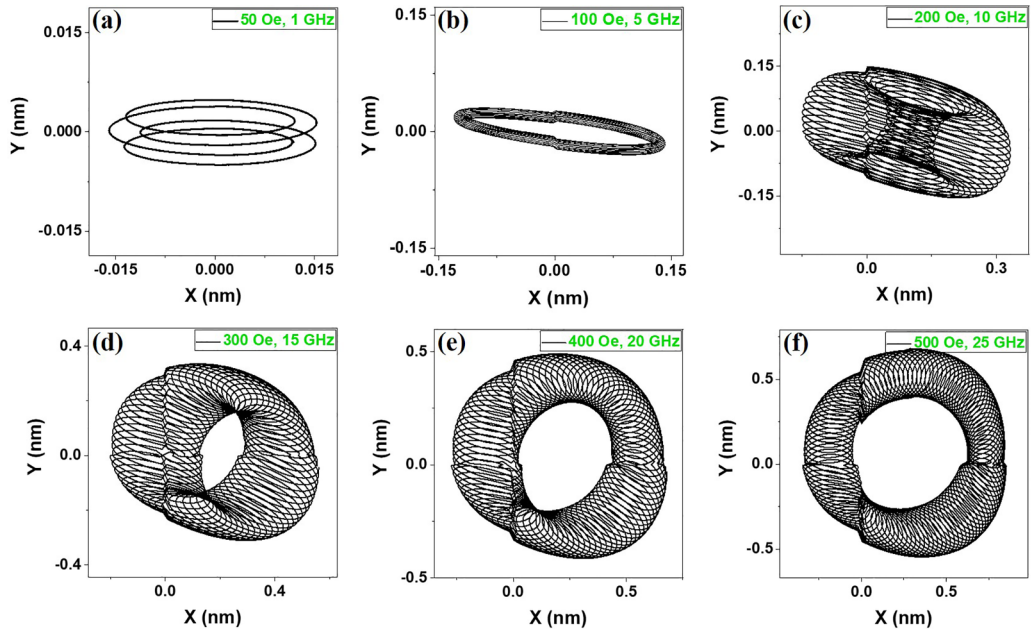


FIG. 7. Driven-motion trajectories of the vortex core (VC) under plane waves excited by $\mathbf{H}_{ac} = h_0 \sin(2\pi ft)\hat{z}$ on the left ~ 512 nm away from the core center with (a) $h_0 = 50$ Oe, $f = 1$ GHz; (b) $h_0 = 100$ Oe, $f = 5$ GHz; (c) $h_0 = 200$ Oe, $f = 10$ GHz; (d) $h_0 = 300$ Oe, $f = 15$ GHz; (e) $h_0 = 400$ Oe, $f = 20$ GHz; and (f) $h_0 = 500$ Oe, $f = 25$ GHz. The plane-wave front is as wide as 1024 nm.

Fig. 7, we show several representative motion patterns of the core under constant pumping of SWs in different amplitudes and frequencies (notably, according to our observations, for a fixed frequency, increase of field intensity h_0 results in approximately unchanged pattern but increased dimensional span. On the other hand, for a fixed field intensity, it shows similar patterns as in Fig. 7 for the same frequency series). The patterns exhibit great complexity and largely differ from each other. Nonetheless, we find an accordant sense of rotation among them given the same \mathbf{C} and \mathbf{P} conditions. The sense of rotation follows a simple rule, as tabulated in Fig. 8, which is consistent with Thiele's theory [69] and early experimental findings [68]. In the present case where $(\mathbf{C}, \mathbf{P}) = (+1, -1)$, the motions generally rotate clockwise (CW).

As known, deviation of the VC from equilibrium induces magnetic charges and largely affects the magnetostatic energy of the vortex system [70,71]. Due to the bowl-shaped

C \ P	-1	+1
	-1	CW
+1	CW	CCW

FIG. 8. Rotation senses of core motion with respect to \mathbf{C} and \mathbf{P} . CW and CCW, respectively, denote clockwise rotation and counter-clockwise rotation.

potential well bound to the vortex, Eq. (2) is no longer sufficient to describe motion of the core in the disk. To comprehend the various patterns in Fig. 7, we carry out fast Fourier transform (FFT) analysis to the temporal variations of the core position over considerable periods. The obtained FFT power spectra in the frequency domain reveal two prominent peaks: an ever-present low frequency of 0.24 GHz and a high frequency exactly the same as the pumping SWs, see Fig. 9. The FFT intensities in different cases largely differ. However, in each case, for the 0.24 GHz, the

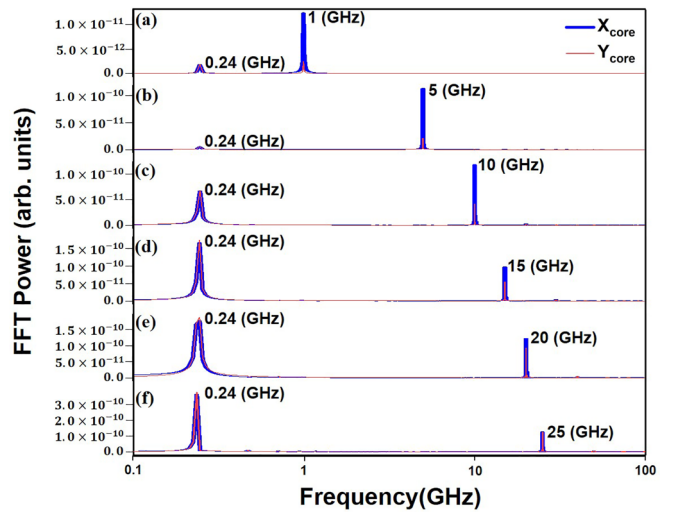


FIG. 9. Fast Fourier transform (FFT) spectra of the driven motions of the vortex core (VC) corresponding to Fig. 7 in alphabetical order. The FFT of the X and Y components are respectively labeled with blue and red curves. The scale of the x axis is of \log_{10} type.

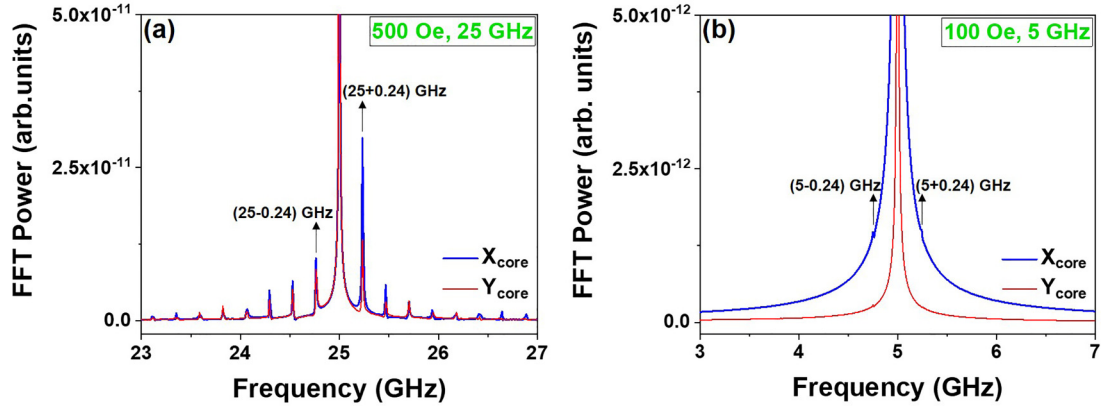


FIG. 10. (a) Zoomed-in fast Fourier transform (FFT) spectrum of the driven motion of the vortex core (VC) ~ 25 GHz for ($h_0 = 500$ Oe, $f = 25$ GHz). (b) Zoomed-in FFT spectrum of the driven motion of VC ~ 5 GHz for ($h_0 = 100$ Oe, $f = 5$ GHz). The FFT of the X and Y components are respectively labeled with blue and red curves.

X, Y components are of the same amplitude, which suggests a circular motion of the VC. For the high frequency though, FFTs of the two components appear to be different, hence an elliptical motion of the core, which is like observations in the study of the vortex in cross-structure waveguides [29]. A close look at the FFT spectra further reveals a series of minor peaks, see for example, Fig. 10(a), which shows a zoomed-in image of Fig. 9(f) ~ 25 GHz. Since the frequencies can be expressed as $25 \pm 0.24n$ GHz, where n denotes an integer, these minor peaks may arise from the nonlinear couplings of the two modes of motion [45]. The intensities of such mixed modes depend on the amplitudes of the original circular and elliptical modes. As

seen in Fig. 10(b), which shows the zoomed-in image of Fig. 9(b) ~ 5 GHz, the first-order 25 ± 0.24 GHz appears to be extremely small, and the higher orders are barely observed as the amplitude of peak 0.24 GHz becomes insignificant in Fig. 9(b).

A visualization of the two basic modes of motion is given in Fig. 11, where one can find varied amplitudes of the circular mode as well as varied amplitudes, ellipticities (i.e., long-to-short axial ratio), and tilting angles of the elliptical mode, with respect to h_0 and ω . In addition to the vivid orbiting motions of the two modes, deviations of motion centers from the disk center (i.e., the averaged in-plane deviation of the VC from the disk center) are also appended, as labeled by

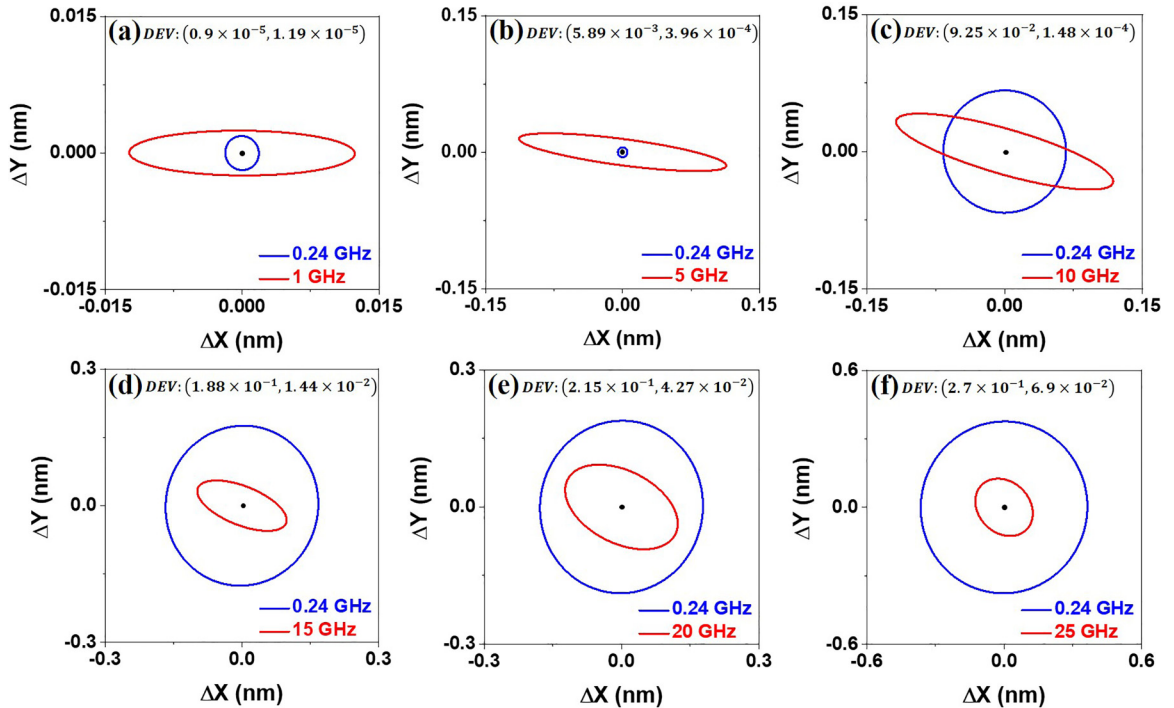


FIG. 11. Corresponding trajectories to the individual fast Fourier transform (FFT) peaks in Fig. 9. Blue and red curves respectively sketch the component circular motion and elliptical motion of the vortex core (VC). DEV denotes the averaged in-plane deviation of VC from disk center.

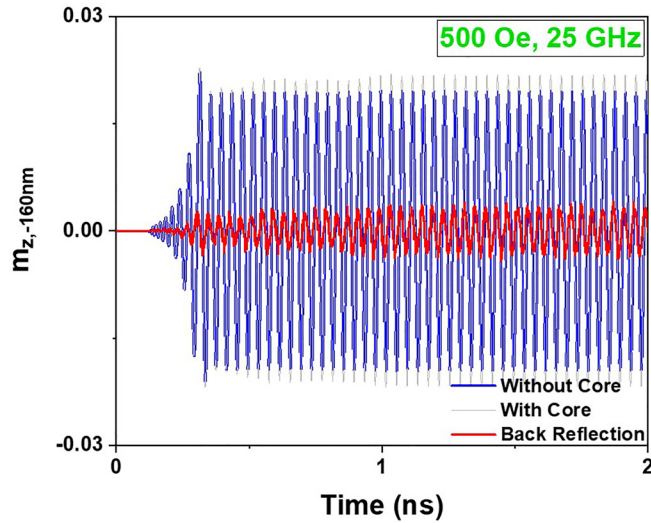


FIG. 12. Normalized magnetization component m_z at 160 nm away from the vortex core (VC) as a function of time. The blue curve denotes the spin-wave (SW) propagation in the absence of a VC, which is obtained based on uniform magnetization since the spin textures in a standard vortex along the radial direction within a certain lateral range can be approximately viewed as uniform. The gray curve denotes the SW propagation in the presence of a VC. The red curve denotes the back reflection of SW by the VC. The SWs are excited based on $h_0 = 500$ Oe and $f = 25$ GHz.

DEV. Notably, in all cases, the motion centers shift to the upper right. The upward DEV can be attributed to the strong skew scattering of SWs. The forward DEV, however, lacks explanation. Considering the common phenomena of SW reflection by the many magnetic solitons (e.g., domain wall) due to rise of dynamic stray field [31,72–74], we compare the arrived SWs at a spot in front of the disk center in cases in absence and in presence of a VC. By subtracting the SW of the former case from that of the latter, we observe clear back reflection of SWs by the VC (see for instance, the red curve in Fig. 12, which is calculated based on the case under $h_0 = 500$ Oe and $f = 25$ GHz), which suggests a process of linear momentum transfer torque (LMTT) [48,72,73]. Note that the highly overlapped magnetization oscillations in the early stage of 0.5 ns between the blue and gray curves indicate basically unchanged propagation of SWs in two cases and evidence the effectiveness of uniform magnetization as an alternative when simulating SW propagation in the absence of a VC. Thus far, one may conclude three scattering behaviors of the propagating SW in vortex: skew scattering, side deflection, and back reflection. The skew scattering and back reflection of SWs together yield steady reaction forces on the core and can further balance with the restoring force provided by the bowl-shaped potential well bound to the vortex. In comparison with the case of a skyrmion, one thus finds similar interactions except the side deflection of SWs which can be ascribed to the widely extended size of the vortex [48].

To understand the motion modes of the VC, further simulation under SWs of 0.24 GHz (as an illustration, the SW is excited based on $h_0 = 50$ Oe and $f = 0.24$ GHz) is priorly performed with recorded trajectory shown in Fig. 13(a). As

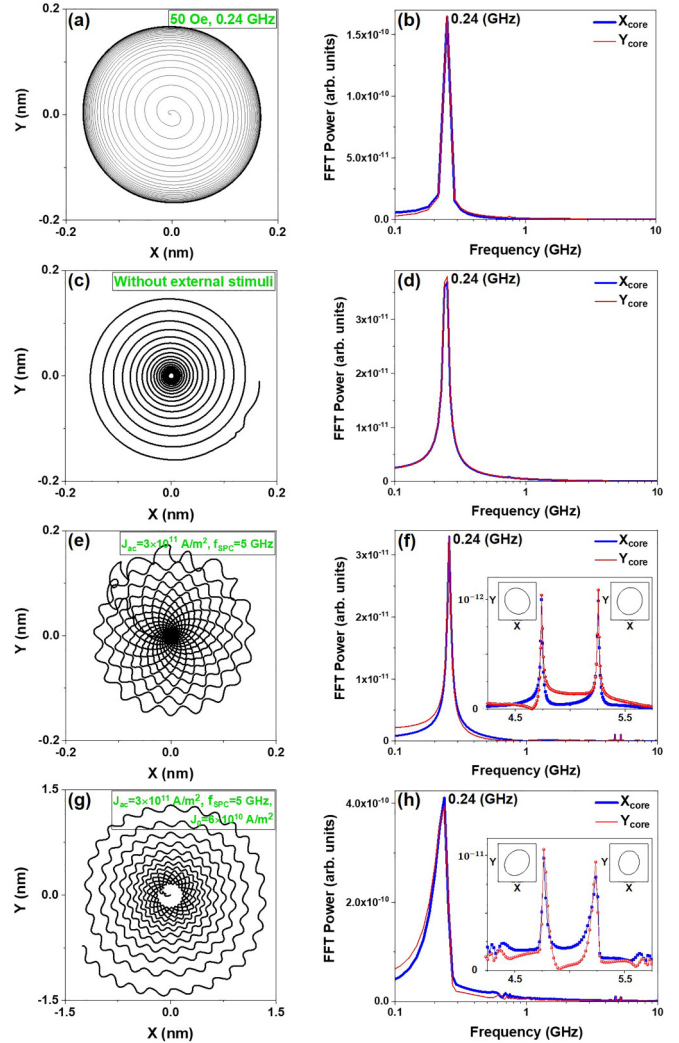


FIG. 13. (a) Motion trajectory (gray curve) of the vortex core (VC) by spin wave (SW) under $h_0 = 50$ Oe and $f = 0.24$ GHz. The black color highlights the limit circle when VC undergoes periodic movement. Motion trajectories of VC under (c) no external stimuli; (e) spin-polarized current of $J_1 = J_{ac} \sin(2\pi f_{SPC}t)$ where $J_{ac} = 3 \times 10^{11} \text{ A m}^{-2}$ and $f_{SPC} = 5$ GHz; and (g) spin-polarized current of $J_2 = J_0 + J_{ac} \sin(2\pi f_{SPC}t)$, where $J_0 = 6 \times 10^{10} \text{ A m}^{-2}$, $J_{ac} = 3 \times 10^{11} \text{ A m}^{-2}$, and $f_{SPC} = 5$ GHz. Note that, in (c), (e), and (g), the cores are initially displaced by a field pulse. The current polarization P , the Slonczewski parameter Λ , and Slonczewski secondary spin-transfer torque (STT) term ε' in the Slonczewski STT model are respectively set to be 0.2, 1, and 0, whereas the unit magnetization vector in the fixed layer is (0, 0, 1). (b) Fast Fourier transform (FFT) spectra corresponding to the periodic circular movement in (a). (d), (f), and (h) FFT spectra of (c), (e), and (g), respectively, showing averaged FFT power. Insets in (f) and (h) demonstrate two mixed modes ~ 5 GHz, in which the ellipticity can be found.

one may expect, excitation of the circular mode at 0.24 GHz is continuously observed. However, the elliptical mode disappears, see the FFT spectrum in Fig. 13(b). Figures 13(c) and 13(d) display the case where the core undergoes naturally damped spiral gyration [75] with the intrinsic frequency that happens to be 0.24 GHz. The coincident peaks in Figs. 13(b)

and 13(d) suggest that the circular mode in fact corresponds to undamped 2D harmonic oscillations of the VC.

To explain how such undamped harmonic oscillations can be sustained, we follow Thiele's formalism [69], which assumes a rigid vortex profile with its internal magnetization characterized solely by VC position \mathbf{X} [i.e., $\mathbf{m}(\mathbf{r}) = \mathbf{m}_0(\mathbf{r} - \mathbf{X})$, where \mathbf{r} denotes the space coordinate, and \mathbf{m}_0 is the initial magnetization distribution when the core locates at the origin]. Considering the spin angular momentum transfer effect, the Thiele equation can be written as

$$\mathcal{G}_{ij}\dot{X}_j = -\partial_i\mathcal{W} + \mathcal{D}_{ij}\dot{X}_j + \mathcal{F}_{ST}^i, \quad (6)$$

where the left-hand-side term represents the gyrotropic force; and the first, second, and third terms on the right side are respectively restoring force (here, \mathcal{W} denotes total magnetic energy), dissipation force, and spin-torque force. Components of the gyrotensor $\hat{\mathcal{G}}$ and dissipation tensor $\hat{\mathcal{D}}$ can be expressed as follows [76]:

$$\mathcal{G}_{ij}(\mathbf{X}) = \frac{M_S}{\gamma} \int d^3\mathbf{r} (\partial_i \mathbf{m} \times \partial_j \mathbf{m}) \cdot \mathbf{m}, \quad (7)$$

$$\mathcal{D}_{ij}(\mathbf{X}) = -\alpha_{LLG} \frac{M_S}{\gamma} \int d^3\mathbf{r} (\partial_i \mathbf{m} \times \partial_j \mathbf{m}). \quad (8)$$

Notably, the gyrotropic and restoring forces are of the radial direction, whereas the dissipation force is perpendicular to the VC displacement [76,77]. Based on the Thiele equation, one immediately learns that, to sustain an undamped circular motion in which $\dot{\mathbf{X}} = \boldsymbol{\omega} \times \mathbf{x}$ holds, the dissipation force must be compensated by a steady spin-torque force. Spin-polarized current (SPC) has been shown to be able to counteract dissipation and successfully maintain circular motion of the VC [76,77]. Specifically, when a SPC flows perpendicularly to the disk plane, the concomitant STT term $\boldsymbol{\tau}_{\text{SPC}} = \sigma \mathbf{J} \mathbf{m} \times (\mathbf{m} \times \mathbf{P})$ gives rise to a spin-torque force [78,79] $\mathcal{F}_{ST}^i(\mathbf{X}) = M_S \sigma J P \int d^3\mathbf{r} (\mathbf{m} \times \partial_i \mathbf{m})$, where $\sigma = \hbar\eta/(2Le|M_S)$, η is current spin polarization, L is free layer thickness, J is current density, and $\mathbf{P} = P\hat{z}$ represents the unit vector of polarizer magnetization ($P = \pm 1$). Obviously, SPC excites VC motion when the electrons bring a magnetic moment from the polarizer to the free layer opposite to the core polarization (i.e., the overall STT $\boldsymbol{\tau}_{\text{SPC}}$ tends to reduce the degree of polarization of the core). Like SPC, a propagating SW through the core can be expected to yield a similar effect. Note that propagation of SWs inevitably causes precession of core magnetization, which naturally involves a process of STT. In Figs. 14(a) and 14(b), we record the core magnetization components subjected to SWs of 0.24 GHz. A gradual enlarging of the precession of the core is clearly accompanied with a monotonous reduction in net core magnetization along the z axis (see the red double-headed arrow), evidencing considerable magnonic STT $\boldsymbol{\tau}_{\text{SW}}$. Based on such a magnonic STT term, sustained circular motion of the VC becomes a natural consequence of the constant SW propagation. As the propagating SW gets stronger, one may further expect an increasing orbiting radius (we will show this below). Interestingly, the ability of SWs in driving such intrinsic circular motion can also be extended to general frequencies, as already demonstrated in Fig. 9, which includes the circular motion as a component mode in the FFT spectrum. According to our theory, one thus expects that there must exist certain net changes in the core magnetization (in

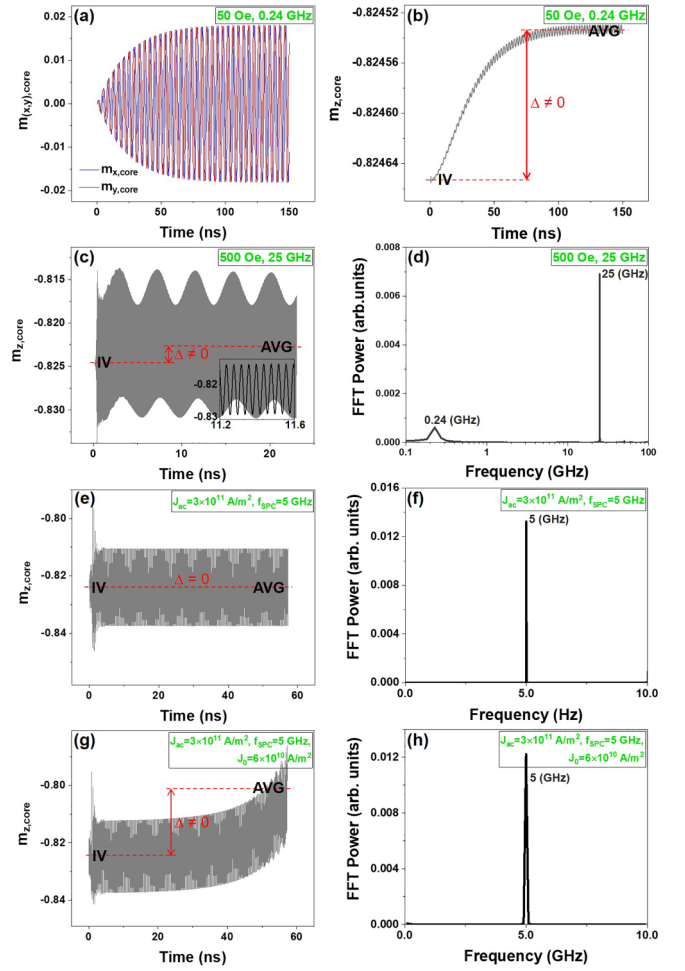


FIG. 14. (a) The x , y components of the vortex core (VC) magnetization as a function of time under spin wave (SW) excited by $h_0 = 50$ Oe, $f = 0.24$ GHz. The z component of VC magnetization as a function of time under (b) SW excited by $h_0 = 50$ Oe, $f = 0.24$ GHz; (c) no external stimuli; (e) spin-polarized current of $J_1 = J_{ac} \sin(2\pi f_{\text{SPC}} t)$, where $J_{ac} = 3 \times 10^{11}$ A m⁻², $f_{\text{SPC}} = 5$ GHz; and (g) spin-polarized current of $J_2 = J_0 + J_{ac} \sin(2\pi f_{\text{SPC}} t)$, where $J_0 = 6 \times 10^{10}$ A m⁻², $J_{ac} = 3 \times 10^{11}$ A m⁻², and $f_{\text{SPC}} = 5$ GHz. IV and AVG respectively abbreviate the initial value and the average of $m_{z,\text{core}}$. Δ denotes the difference between them. (d), (f), and (h) are respectively fast Fourier transform (FFT) spectrums of (c), (e), and (g).

other words, net STT) correspondingly, which is indeed the case as we examine simulations with arbitrary SW propagation. For simplicity, here, we show the case under SWs excited by ($h_0 = 500$ Oe, $f = 25$ GHz), see the nonzero Δ in Fig. 14(c). Thus far, the ever-present excitation of the circular mode can be reasonably understood.

As to the elliptical mode (i.e., orbit with periodically changed radius) by SWs with frequencies other than 0.24 GHz, bearing in mind that constant STT gives rise to perfect circular motion of the core, we reckon that an oscillating STT is herein demanded. Indeed, oscillations of core component magnetization $m_{z,\text{core}}$ can be clearly seen in Fig. 14(c). By FFT analysis, one thus finds an oscillating frequency identical to that of the propagating SW and the elliptical motion, in

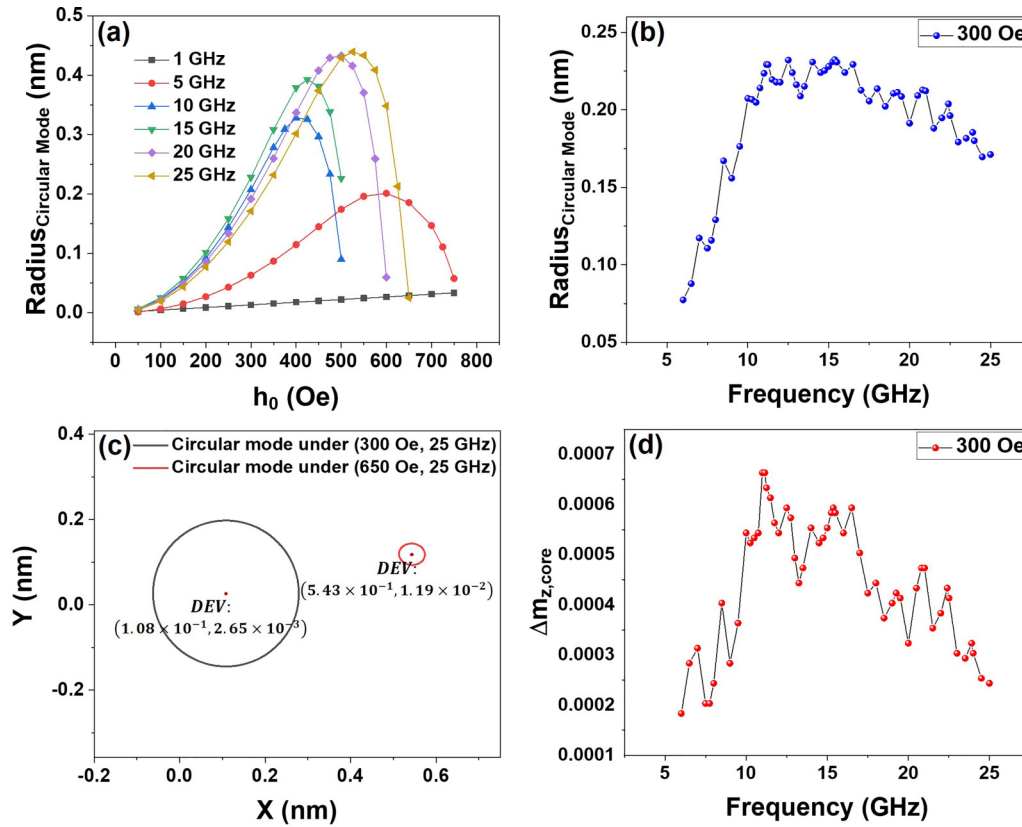


FIG. 15. (a) Radius of circular mode as a function of h_0 (before mode collapse) for several representative frequencies. (b) Radius of circular mode as a function of frequency under fixed h_0 of 300 Oe. Note that the radius is measured along the y axis, and the sampling density is purposely increased around certain h_0 and frequencies to reveal more details. (c) Comparison of the circular modes excited by $h_0 = 300$ Oe, $f = 25$ GHz and $h_0 = 650$ Oe, $f = 25$ GHz. (d) Induced $\Delta m_{z,\text{core}}$ as a function of frequency under fixed h_0 of 300 Oe.

the dominant peak at 25 GHz. The small peak at 0.24 GHz may relate to a periodic distortion of the VC due to periodic displacement of the core away from the disk center [80] (note that the motion center of the circular mode is considerably shifted, hence large oscillations in the core displacement).

To verify the correspondence between the circular mode (elliptical mode) and net STT (oscillating STT), we investigate the driven motion of the VC under ac and dc SPC. In Fig. 13(e), we show the recorded trajectory under a small ac SPC of $J_1 = J_{ac} * \sin(2\pi f_{\text{SPC}}t)$, where $J_{ac} = 3 \times 10^{11}$ A m⁻², and $f_{\text{SPC}} = 5$ GHz. Note that the core is initially displaced by a field pulse and tends to undergo damped spiral gyration until the disk center. Along with the skeletal spiral gyration, small fluctuations at frequencies ~ 5 GHz are clearly stimulated. Like the cases in Fig. 10, mixed modes of 5 ± 0.24 GHz are observed [see Fig. 13(f)], which can be ascribed to the coupling between the intrinsic spiral gyration and the forced synchronous motion by the ac SPC (notably, the absence of the peak of 5 GHz is due to the overwhelmingly larger amplitude of the 0.24-GHz gyration compared with the 5-GHz motion). Nevertheless, the obvious ellipticity effect in each mixed mode can be observed. Similar results are also found under SPC containing both ac and dc components, see Figs. 13(g) and 13(h), where we have applied SPC of $J_2 = J_0 + J_{ac} \sin(2\pi f_{\text{SPC}}t)$, where $J_0 = 6 \times 10^{10}$ A m⁻², $J_{ac} = 3 \times 10^{11}$ A m⁻² and $f_{\text{SPC}} = 5$ GHz. The dc component

functions to trim the orbiting radius until new equilibrium, which is consistent with early studies [76,77,81]. The corresponding $m_{z,\text{core}}$ profiles with respect to SPCs J_1 and J_2 are displayed in Figs. 14(e) and 14(g). Indeed, the ac SPC causes no net changes in $m_{z,\text{core}}$ (hence no net STT) but oscillations (hence only oscillating STT) with frequency being the same as that of the injecting SPC [see Fig. 14(f)]. To summarize, we confirm the causality between the elliptical mode (circular mode) and oscillating STT (net STT). The SW is equivalent to SPC containing both dc and ac components, which respectively exerts net STT and oscillating STT and further excites the circular and elliptical modes of the VC. The frequency of the circular mode is the same as the intrinsic frequency of natural spiral gyration, whereas the frequency of the elliptical mode is consistent with that of the SW propagating through the VC.

To obtain comprehensive knowledge about the two modes, we further scan the (h_0, ω) space for the essential characters therein. In Fig. 15(a), we show the radius of the circular mode with respect to h_0 (or amplitude of the SW) at several representative frequencies. The radius initially increases with h_0 , as expected. However, in each case, there exists a certain threshold beyond which the radius starts to drop. This may ascribe to changes in residing potential due to the large displacement of the VC from the disk center and hence altered dynamics based on the Thiele formalism. Conceivably, a large displacement

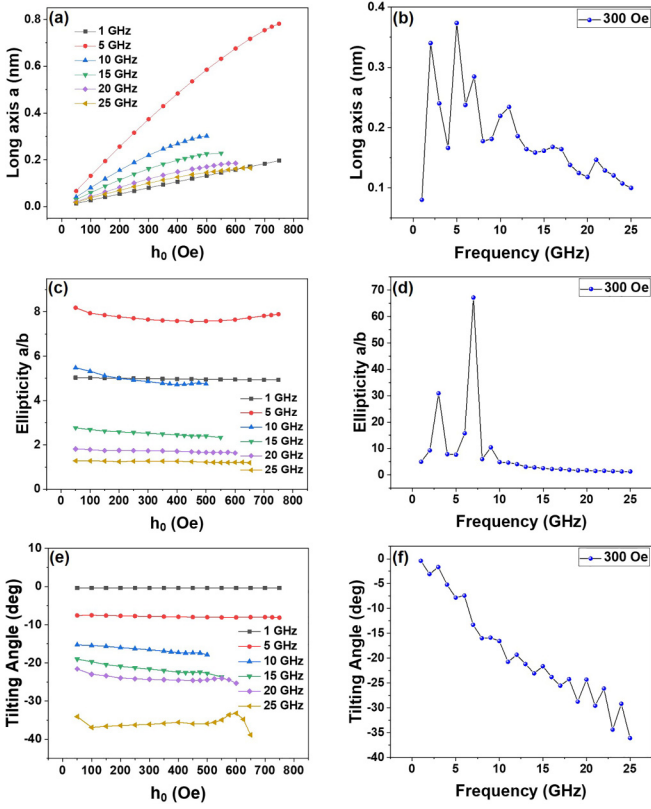


FIG. 16. The long axis of the elliptical mode as a function of (a) h_0 for several representative frequencies and (b) frequency under fixed h_0 of 300 Oe. The ellipticity of the elliptical mode as a function of (c) h_0 for several representative frequencies and (d) frequency under fixed h_0 of 300 Oe. The tilting angle of the elliptical mode as a function of (e) h_0 for several representative frequencies and (f) frequency under fixed h_0 of 300 Oe. (a), (c), and (e) are plotted based on the same sampling points as in Fig. 15(a). The sampling points in (b), (d), and (f) are evenly spaced with intervals of 1 GHz.

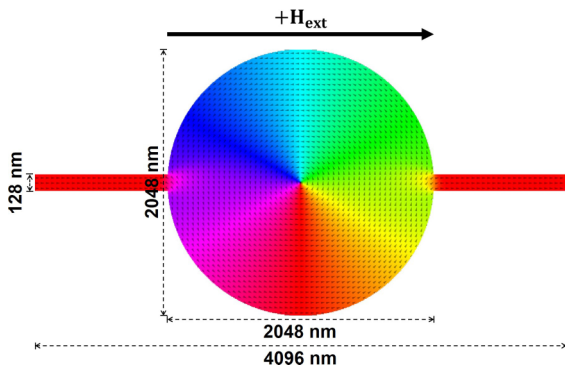


FIG. 17. Schematic of vortex-based spin-wave (SW) valve (VSV) in which propagating SWs can be switched on and off by shifting the vortex core (VC) position. For simplicity, the diameter of the disk is 2048 nm (i.e., $R = 1024$ nm), and the width of the interconnecting strip is set to be 128 nm. The switch-off field is determined to be -5.85 Oe that points to the left. In the remaining content, SWs will be excited in the middle of the left branch of the nanostrip.

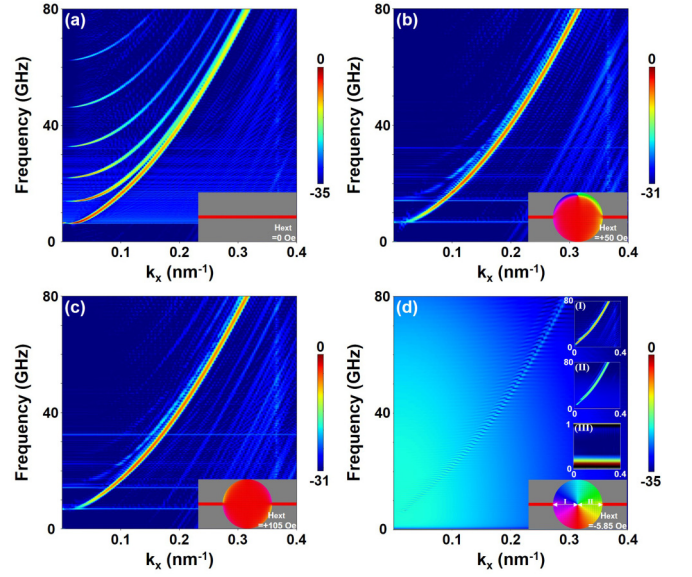


FIG. 18. Dispersion of spin wave (SW) within interval $[-R, R]$ ($R = 1024$ nm) in (a) thin-film nanostrip with width of 128 nm, (b) proposed vortex-based SW valve (VSV) when switching on with an external field of $+50$ Oe, (c) proposed VSV when the vortex is annihilated under an annihilation field of $+105$ Oe, and (d) proposed VSV when switching off with switch-off field of -5.85 Oe. Insets I and II respectively plot the dispersions within $[-R, -0.01R]$ and $[0.01R, R]$ which exclude the VC. As seen, the lowest band can be more easily identified. Inset III shows the zoomed-in image of the dispersion within $[-R, R]$ in the narrow frequency range of $[0, [1]]$ GHz. The dispersions are calculated based on SW excitation by a sine cardinal (Sinc) function field, using MuFA [82]. To eliminate the SW reflection, absorbing boundary conditions are continuously adopted near the disk edge.

can originate from three sources: (i) a large DEV due to strong skew scattering and/or back reflection, (ii) a large amplitude of the elliptical mode, and (iii) a large amplitude of the circular mode itself. In Fig. 15(c), we demonstrate a case conforming to the first scenario, in which one finds significant reduction of the orbiting radius for a larger DEV. Notably, in addition to the reduced radius, the circular mode may even be deformed and transformed into the elliptical mode. From Fig. 15(a), one

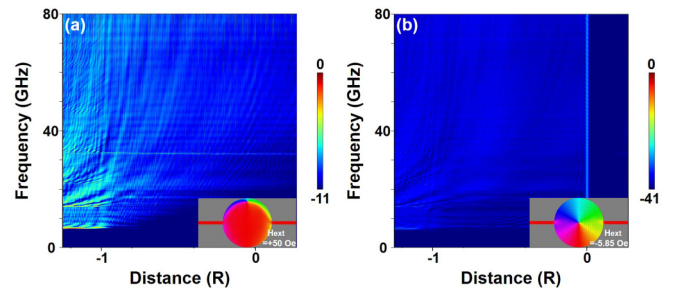


FIG. 19. (a) Spectrum of spin-wave (SW) propagation corresponding to Fig. 18(b). (b) Spectrum of SW propagation in proposed vortex-base SW valve (VSV) when switching off. R denotes the radius of the disk and is 1024 nm. 0 and -1 on the x axis respectively indicate the center and the left boundary of the disk.

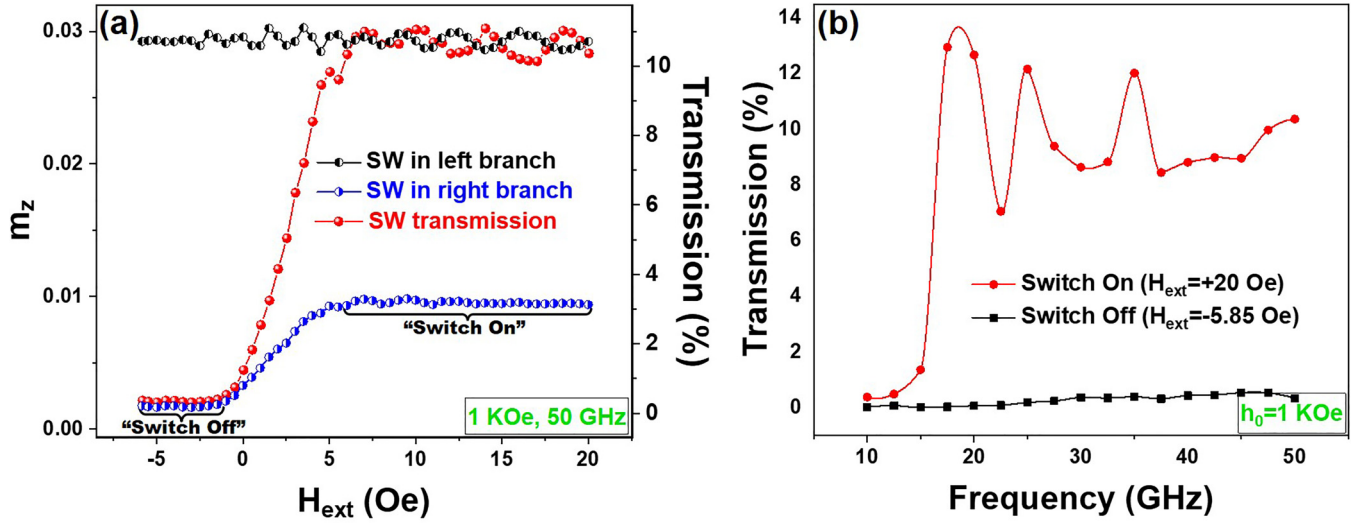


FIG. 20. (a) Incoming spin wave (SW) in the left branch (viz., $x = -1280$ nm), outgoing SW in the right branch (viz., $x = 1280$ nm), and the corresponding transmission as a function of external field H_{ext} . SWs are excited based on $h_0 = 1$ kOe, $f = 50$ GHz. (b) SW transmission as a function of SW frequency f under switch-on field of $+20$ Oe and switch-off field of -5.85 Oe. SWs are excited based on $h_0 = 1$ kOe.

can also sense apparent frequency dependence of the circular mode radius, which has been plotted in detail in Fig. 15(b) for case $h_0 = 300$ Oe. The radius majorly increases in the low band and decreases in the relatively higher band with respect to frequency, while accompanied with multiple peaks. Strikingly, in Fig. 15(d), we find exactly coincident peaks in the $\Delta m_{z,\text{core}}$ spectrum, which again evidence the net STT mechanism of propagating SWs in exciting circular modes. The peaks throughout the spectrum, on the other hand, suggest the effect of resonance.

Characters of the elliptical mode (including amplitude, ellipticity, and tilting angle) with respect to h_0 and ω , are displayed in Fig. 16. Clearly, the amplitude increases with h_0 following approximately a linear function, see Fig. 16(a). The slight bending at large h_0 may likewise be attributed to the large displacement of the VC from the disk center. For the same h_0 , amplitudes at different frequencies further differ, and in Fig. 16(b), one finds dominant peaks at 2, 5, 7, 11, 16,

and 21 GHz, suggesting a resonant effect of the oscillating magnon STT. The ellipticity and tilting angle, on the other hand, remain basically constant as h_0 varies, see Figs. 16(c) and 16(e). Notably, these two characters also appear to be frequency dependent. Dominant resonant peaks of 3, 7, and 9 GHz are identified for ellipticity, whereas the tilting angle

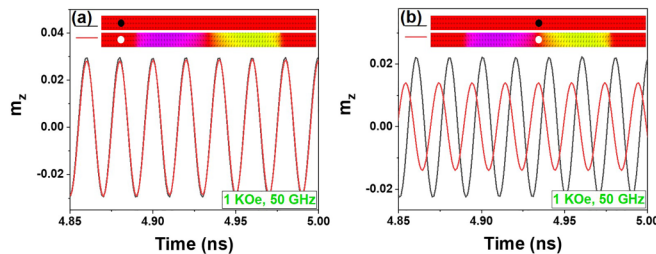


FIG. 21. Comparison between magnetization oscillations (a) at location (viz., $x = -1280$ nm) near the left boundary, (b) at the center of the disk (viz., $x = 0$ nm) in the valve (see the white dots) and at the same locations in the absence of the disk (see the black dots). Attached lower strips depict the inhomogeneous magnetizations within the intersection area of the disk and interconnecting nanostrip under zero H_{ext} , in contrast to the uniform magnetization in the upper comparative strips. Spin waves (SWs) are excited under $h_0 = 1$ kOe and $f = 50$ GHz.

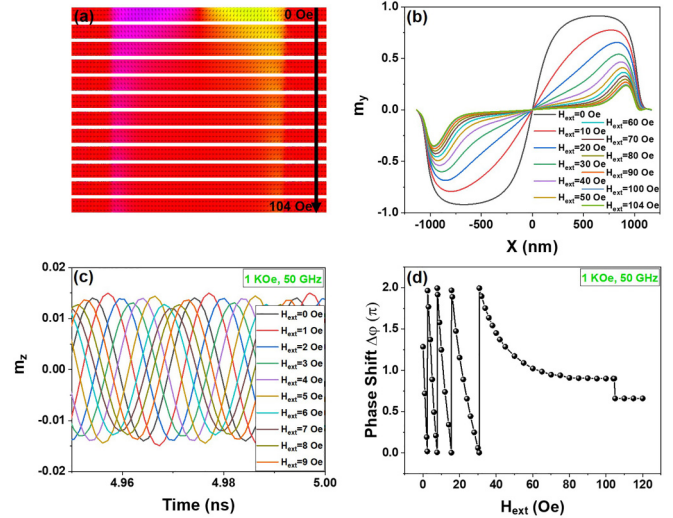


FIG. 22. (a) Spin textures within the intersection area between the disk and the interconnecting nanostrip in vortex-based spin-wave (SW) valve (VSV) with respect to external magnetic field H_{ext} . (b) The m_y profiles corresponding to the spin textures in (a). (c) Recorded magnetization oscillations at the same location as in Fig. 21(b) for different H_{ext} fields of 0, +1, +2, +3, +4, +5, +6, +7, +8, and +9 Oe under SW propagations excited by $h_0 = 1$ kOe and $f = 50$ GHz. (d) Calculated phase shift $\Delta\phi$ of SW after transmission through the entire vortex as a function of H_{ext} . Note that the phase shift is evaluated with respect to uniform magnetization under zero H_{ext} . The positive value of phase shift $\Delta\phi$ corresponds to the backward (or leftward) translation of the $m_z(t)$ curve in the time domain.

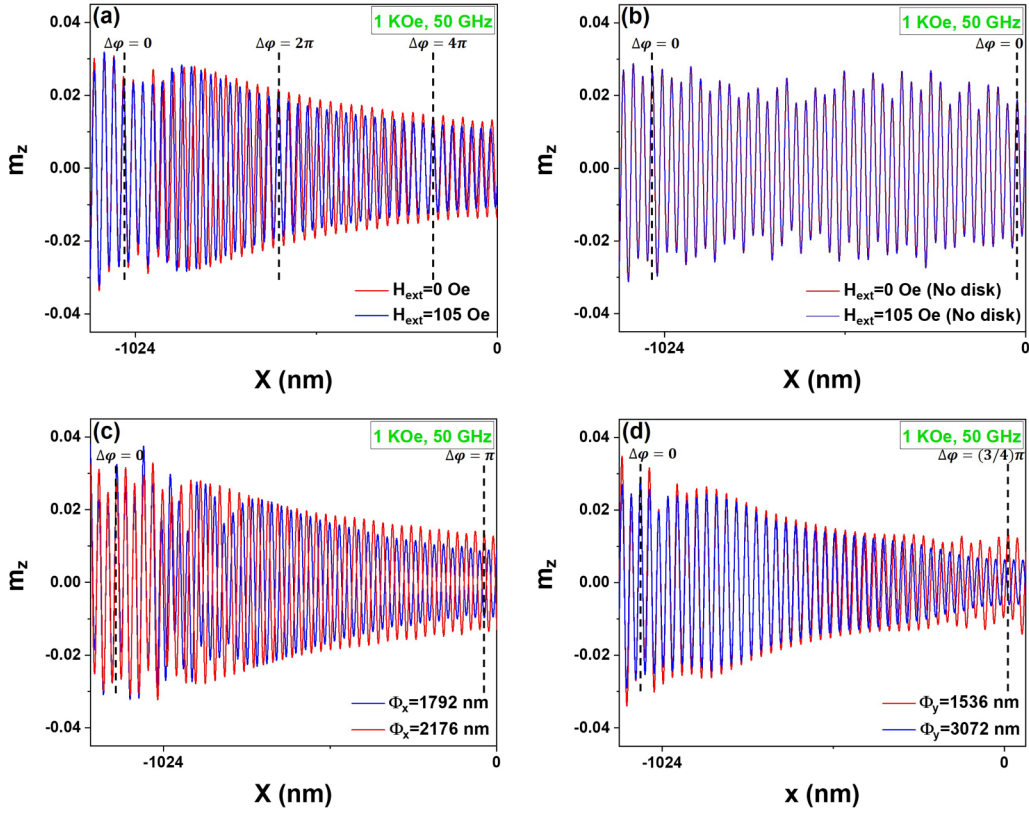


FIG. 23. Comparison of spin-wave (SW) snapshots between (a) cases of proposed vortex-based SW valve (VSV) containing a 2048-nm-diameter disk with $H_{\text{ext}} = 0$ and 105 Oe, (b) cases of mere nanostrip with $H_{\text{ext}} = 0$ and 105 Oe, (c) cases of modified VSV with x -axis diameter $\Phi_x = 1792$ and 2176 nm under zero external field, and (d) cases of modified VSV with y -axis diameter $\Phi_y = 1536$ and 3072 nm under zero external field. SWs are excited based on $h_0 = 1$ kOe and $f = 50$ GHz.

generally decreases with frequency but with small ups and downs.

IV. VORTEX-BASED SW VALVE

In view of the multiscatterings of SWs by vortex and limited displacement of the VC in translational modes by SW propagation over a wide range of frequencies and intensities [note that the VC displacement is typically <1 nm, see Figs. 15(a), 15(b), 16(a), and 16(b)], the vortex is highly promising for realization of a SW valve [hence a vortex-based SW valve (VSV)]. In Fig. 17, we show a possible design with simple geometry in which the VC acts as a switch. The propagating SWs can be switched on and off as we shift the position of the core, which can be done using an external in-plane dc magnetic field H_{ext} (note that such a magnetic field can be easily created by dc electric current flowing in a vertically placed wire). The joint between the disk and the interconnecting nanostrip breaks the tangent magnetization distribution at the disk edge; hence, the VC spontaneously shifts off center (note that magnetizations inside the strip without strong magnetocrystalline anisotropy align in parallel with the longitudinal direction of the strip to minimize magnetostatic energy). Thus, to block the SW, one ought to apply a resetting field that pulls the VC exactly back to the disk center. In the case of Fig. 17 with vortex chirality $\mathbf{C} = +1$ and branch magnetization pointing to the right (i.e., $m_x = +1$), the VC spontaneously shifts into the north semicircle, and the

resetting field is determined to be -5.85 Oe, which points to the left. On the other hand, to channel SWs, a large enough positive switch-on field (but less than the annihilation field) can be used to largely displace the VC and to avoid formation of a prominent wall at the boundaries. It is worth emphasizing that reversing the value of $\mathbf{C} * m_x$ shall reverse the resetting field and the switch-on field.

The dispersion relation of SWs when switching on the VSV has been plotted in Fig. 18(b), in which we have largely deviated the core by an external field of $+50$ Oe, see inset of Fig. 18(b). In contrast to the case without the disk [see Fig. 18(a)], the higher bands clearly vanish. The lowest band, however, remains robust and preserves its parabolic shape, ensuring basically unchanged properties of the transmitting SWs. It is worth mentioning that we find nearly identical dispersions for different cases respectively under fields of $+50$ [see Fig. 18(b)], $+60$, $+70$, $+80$, $+90$, $+100$, and $+105$ Oe [see Fig. 18(c)]. Considering almost the same textures in the intersection area under $+50$, $+60$, $+70$, $+80$, $+90$, and $+100$ Oe [see Fig. 22(b)] and removal of noncollinear texture under annihilation field of $+105$ Oe, one can conclude that the dispersion is not markedly affected by the field amplitude or magnetization texture. The dispersion plot when VSV is switched off under -5.85 Oe is shown in Fig. 18(d). As seen, the lowest band preserves. However, its excitation is clearly overwhelmed by the extremely low-frequency modes that relate to excitation of the VC, see inset III of Fig. 18(d).

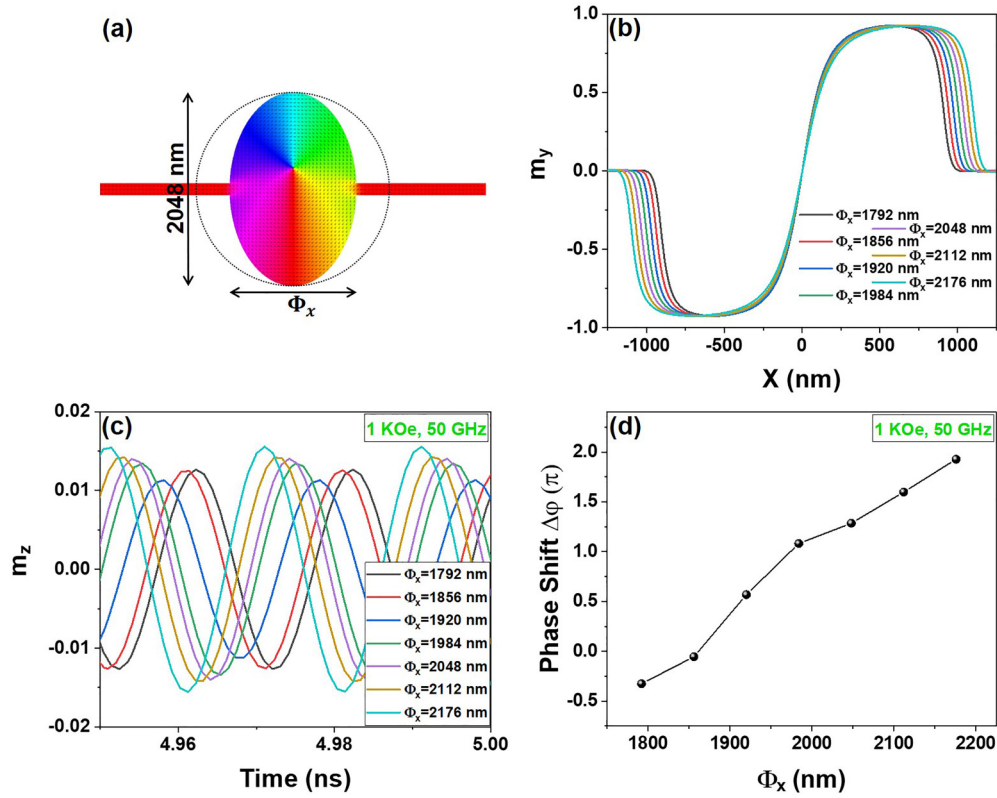


FIG. 24. (a) Schematic of vortex-based spin-wave (SW) valve (VSV) with changed x -axis diameter Φ_x . (b) m_y profiles with respect to several representative Φ_x . (c) Recorded magnetization oscillations at the same location as in Fig. 21(b) for the representative Φ_x under $H_{\text{ext}} = 0$ Oe. SWs are excited based on $h_0 = 1$ kOe and $f = 50$ GHz. (d) Evaluated phase shift $\Delta\phi$ of SW after transmission through the entire vortex as a function of Φ_x . Note that the phase shift is evaluated with respect to uniform magnetization under zero H_{ext} . The negative value of phase shift $\Delta\phi$ corresponds to the forward (or rightward) translation of the $m_z(t)$ curve in the time domain.

The spectrum of SW propagation corresponding to Fig. 18(b) is shown in Fig. 19(a), where one observes typical prohibitions of SWs in the low-frequency range of $[0, 7]$ GHz [83,84], and, most importantly, successful transmission of SWs at higher frequencies. Nonetheless, in the case when the valve is switched off under $H_{\text{ext}} = -5.85$ Oe (i.e., the VC locates at the center of the disk), the VC exhibits good shielding effect on SWs over the entire frequency range, while itself being locally excited [see Fig. 19(b)], which is consistent with Fig. 18(d). To quantify the performance of the VSV, in Fig. 20(a), taking SW excitation under $h_0 = 1$ kOe and $f = 50$ GHz as an example, we evaluate the SW transmission under changed external field H_{ext} . The SW transmission is defined as $T = [(m_{z,R})/(m_{z,L})]^2$, where $m_{z,L}$ and $m_{z,R}$ respectively represent averaged amplitudes of excited SWs in the left branch and transmitted SWs in the right branch [51]. We identify a clear switch-off field range (-5.85 Oe $\leq H_{\text{ext}} \leq -1$ Oe) in which the transmission is $<0.5\%$ and a switch-on field range ($H_{\text{ext}} \geq 6$ Oe) in which the transmission is generally $>10\%$. Notably, for a given switch-on field, the transmission can be highly frequency dependent, whereas for a given switch-off field, the transmission remains low and is not significantly affected by frequency, see Fig. 20(b). Based on Figs. 18–20, we confirm the excellent performance of the vortex as a SW valve.

To better meet technological demand in SW computing, it is necessary to examine the wave character of phase as a

SW transmits through the vortex. Based on $h_0 = 1$ kOe and $f = 50$ GHz, to avoid confusion caused by SW reflection from the edge of the right branch, in Fig. 21, we show the recorded magnetization as a function of time, respectively, at a location near the left boundary and at the center of the disk (see red curves), in contrast to that of a uniformly magnetized nanostrip (see black curves). Note that, in both cases, no H_{ext} fields are applied. Clearly, inhomogeneous spin texture causes a phase shift of SWs. The phase shift has no concern with the direction of noncollinear magnetizations, and therefore, it can be expected to accumulate even though there is no net rotation of in-plane magnetization (hence, the phase shift near the right boundary can be expected to double), which renovates our early knowledge based on studies of domain walls [32,54,64,85,86]. This further suggests that, to calculate the exact phase shift of the SW after long-distance propagation, one necessarily follows the track and takes account of every local magnetization inhomogeneity along the trajectory instead of simply evaluating the topological index of the winding number, which can be extremely important as it, to a large extent, determines future technological development for the information processing based on the SW phase.

Since spin texture can be diversely inhomogeneous in magnetic media, the phase shift with respect to different textures subsequently comes into the next question. In the case of a VSV, we are mostly concerned with the contouring texture within the intersection area between the disk and the nanostrip

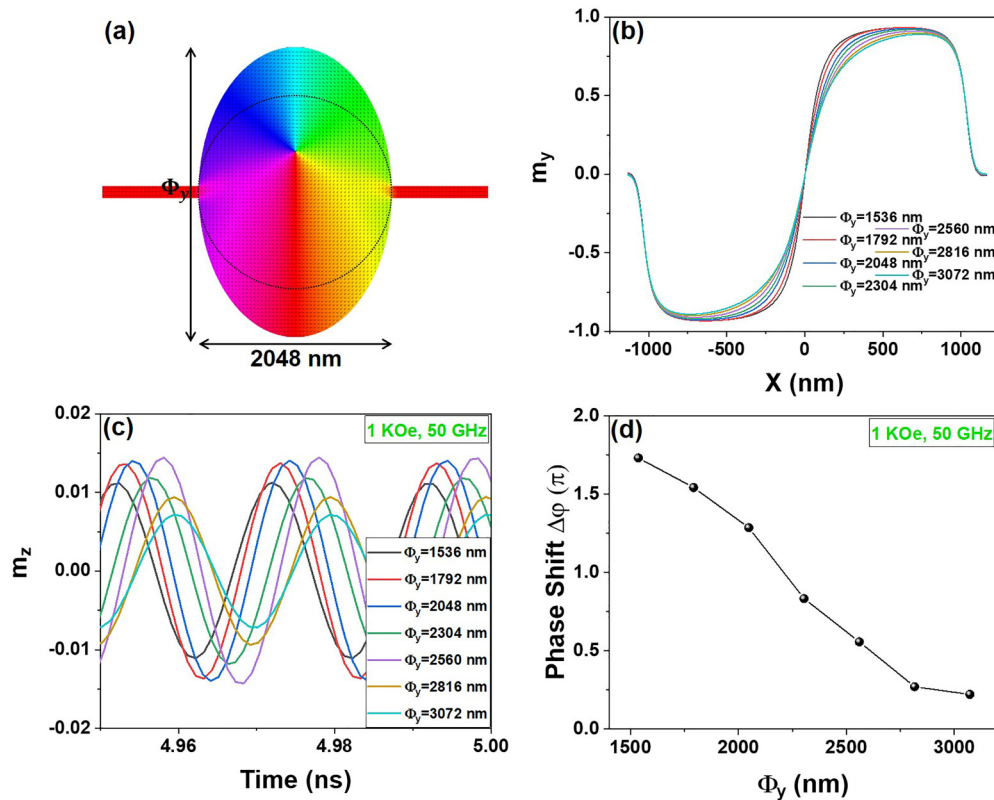


FIG. 25. (a) Schematic of vortex-based spin-wave (SW) valve (VSV) with changed disk y -axis diameter Φ_y . (b) m_y profiles with respect to several representative Φ_y 's. (c) Recorded magnetization oscillations at the same location as in Fig. 21(b) for the representative Φ_y under $H_{\text{ext}} = 0$ Oe. SWs are excited continuously using $h_0 = 1$ kOe and $f = 50$ GHz. (d) Evaluated phase shift $\Delta\phi$ of SW after transmission through the entire vortex as a function of Φ_y . Note that the phase shift is evaluated with respect to uniform magnetization under zero H_{ext} .

under different fields H_{ext} and the corresponding phase shifts of SWs (note that different displacements of the VC correspond to different spin textures in the intersection area). In Fig. 22(a), we show a clear evolution of the spin texture within the intersection area subjected to gradually increased H_{ext} along the $+x$ direction. A demonstration of varying degrees of phase shift under different H_{ext} 's is given in Fig. 22(c). To be more quantitative, the phase shifts after transmission through the entire vortex are evaluated and scanned over a wide range of H_{ext} 's, see Fig. 22(d). Remarkably, in contrast to the discrete phase shift reported in many solitonic textures (e.g., domain walls) [54,85], here, we obtain a smooth phase shift before annihilation based on continuous modulation of the spin texture, and the phase shift clearly covers the entire phase range of $[0, 2\pi]$, which can result in enhanced flexibility even with new functionalities in future device design. It is worth mentioning that, when H_{ext} reaches the critical annihilation field (in this case, it is determined to be $\sim +105$ Oe), the disk magnetization will be saturated, which leads to a cutoff in the phase shift. The nonzero phase shift for fields beyond the annihilation field indicates an imperfectly uniform magnetization in the intersection area. To deepen our understanding regarding the rise of the phase shift in the inhomogeneous spin texture, in Fig. 23(a), we compare the snapshots of SW propagation in cases under zero field and under an annihilation field of $+105$ Oe. Clearly, in the former case with greater inhomogeneity, the SW has an enlarged wavelength (hence larger velocity), which results in an evi-

dent forward (or rightward) phase shift in the spatial domain [equivalently, backward translation of the $m_z(t)$ curve in the time domain]. Notably, in cases with unchanged spin texture, change of the external field only seems to have no effect on shifting the SW phase, see Fig. 23(b). This is consistent with our earlier findings in the study of magnetic domain walls [53] and suggests a general correlation between the SW phase shift and magnetization inhomogeneity. To find out the exact determinants for the phase shift, in Fig. 22(b), we plotted the m_y profiles corresponding to the textures in Fig. 22(a). Comparison between Figs. 22(b) and 22(d) suggests that the phase shift closely relates to the dimensional span of nonzero m_y and the magnitude of m_y .

In the following, we investigate the partial correlation between the phase shift and (i) the dimensional span of nonzero m_y and (ii) the magnitude of m_y . In Fig. 24(a), VSVs with varied disk x -axis diameter Φ_x are simulated under $H_{\text{ext}} = 0$ Oe. The m_y profiles in the intersection area between the modified disks and the interconnecting nanostrip are plotted in Fig. 24(b). Clearly, the nonzero m_y profile decreases its x -axis span as Φ_x decreases but keeps its amplitude and shape nearly unchanged. The vivid shifting of the SW phase and the evaluated phase shifts after transmission through the entire vortex are plotted respectively in Figs. 24(c) and 24(d), from which we confirm the phase shift as a monotone increasing function of dimensional span of the nonzero m_y profile. Comparison of the snapshots of SW propagation for cases with $\Phi_x = 1792$ and 2176 nm again suggests that greater inhomogeneity (in

this case, wider dimensional span of nonzero m_y) gives larger SW wavelength, hence larger forward phase shift in the spatial domain, see Fig. 23(c).

A similar investigation is carried out for VSVs with changed disk y -axis diameter Φ_y under $H_{\text{ext}} = 0$ Oe, see Fig. 25(a). In this case, the magnitude of m_y near the disk center decreases with increasing Φ_y . However, the dimensional span of nonzero m_y remains strictly unchanged, see Fig. 25(b). Based on observations of the phase shift, as shown in Figs. 25(c) and 25(d), we confirm that the phase shift is a monotonically decreasing function of Φ_y or a monotonically increasing function of m_y magnitude. Comparison of the snapshots of SW propagation for cases with $\Phi_y = 1536$ and 3072 nm [see Fig. 23(d)] again evidences the correlation between inhomogeneity and phase shift, as in Figs. 23(a) and 23(c). Specifically, the higher the m_y magnitude, the larger the SW wavelength (hence larger forward phase shift in spatial domain).

V. CONCLUSIONS

In conclusion, the interaction between propagating SWs and Heisenberg vortex in a ferromagnetic disk has been studied. We found three distinct scattering behaviors of SWs: namely, the unilateral skew scattering, symmetric side deflection, and back reflection, which respectively associate with the magnetic topology, the local energy density distribution of the texture, and the LMST. The skew scattering is well confined within the VC and is polarity dependent. The side deflection mainly occurs in the out-of-core region and can be tuned through modifications in size or geometry of the spin system.

On the other hand, the VC under steady impinging of magnons exhibits two translational modes: the intrinsic circular and coercive elliptical modes. The former was found to be a result of net magnonic STT effect, whereas the latter can be ascribed to a process of oscillating magnonic STT. The essential characters of the two modes generally manifest as a resonant effect in the frequency domain. The amplitude additionally demonstrates strong field dependence. Coupling of the two modes can further result in a frequency comb.

One step further, by utilizing the multiple scatterings of SWs and immobility of the VC, we propose a SW valve based on the vortex, which enables excellent SW valving performance and smooth phase control via inhomogeneity modulation. The phase shift arises from the enlarged wavelength of SWs when propagating in inhomogeneous textures and is determined to be a monotonically increasing function of both the magnitude and the dimensional span of the inhomogeneity of the contouring texture regardless of its winding number, which renovates previous understanding. Our findings shall deepen the understanding toward the interplay between SWs and magnetic textures and advance the development of magnonic devices.

ACKNOWLEDGMENTS

This paper is supported by the National Natural Science Foundation of China (Grants No. 12074332, No. 12074057, No. 11974250, No. 62175155, and No. 52172005), the National Key Research and Development Program of China under Contract No. 2022YFA1402802, and the Training Program of National Natural Science Foundation of China (Grant No. SK202206).

-
- [1] F. Bloch, Zur theorie des ferromagnetismus, *Z. Physik* **61**, 206 (1930).
- [2] T. Holstein and H. Primakoff, Field dependence of the intrinsic domain magnetization of a ferromagnet, *Phys. Rev.* **58**, 1098 (1940).
- [3] F. J. Dyson, General theory of spin-wave interactions, *Phys. Rev.* **102**, 1217 (1956).
- [4] V. V. Kruglyak, S. O. Demokritov, and D. Grundler, Magnonics, *J. Phys. D: Appl. Phys.* **43**, 264001 (2010).
- [5] A. V. Chumak, V. I. Vasyuchka, A. A. Serga, and B. Hillebrands, Magnon spintronics, *Nat. Phys.* **11**, 453 (2015).
- [6] B. Lenk, H. Ulrichs, F. Garbs, and M. Münzenberg, The building blocks of magnonics, *Phys. Rep.* **507**, 107 (2011).
- [7] T. Shinjo, T. Okuno, R. Hassdorf, K. Shigeto, and T. Ono, Magnetic vortex core observation in circular dots of permalloy, *Science* **289**, 930 (2000).
- [8] A. Wachowiak, J. Wiebe, M. Bode, O. Pietzsch, M. Morgenstern, and R. Wiesendanger, Direct observation of internal spin structure of magnetic vortex cores, *Science* **298**, 577 (2002).
- [9] A. M. Kosevich, B. A. Ivanov, and A. S. Kovalev, Magnetic solitons, *Phys. Rep.* **194**, 117 (1990).
- [10] B. Van Waeyenberge, A. Puzic, H. Stoll, K. W. Chou, T. Tyliczszak, R. Hertel, M. Fähnle, H. Brückl, K. Rott, G. Reiss *et al.*, Magnetic vortex core reversal by excitation with short bursts of an alternating field, *Nature (London)* **444**, 461 (2006).
- [11] B. Pigeau, G. de Loubens, O. Klein, A. Riegler, F. Lochner, G. Schmidt, and L. W. Molenkamp, Optimal control of vortex-core polarity by resonant microwave pulses, *Nat. Phys.* **7**, 26 (2011).
- [12] S. Wintz, V. Tiberkevich, M. Weigand, J. Raabe, J. Lindner, A. Erbe, A. Slavin, and J. Fassbender, Magnetic vortex cores as tunable spin-wave emitters, *Nat. Nanotechnol.* **11**, 948 (2016).
- [13] R. Hertel and C. M. Schneider, Exchange Explosions: Magnetization Dynamics During Vortex-Antivortex Annihilation, *Phys. Rev. Lett.* **97**, 177202 (2006).
- [14] S. Choi, K. S. Lee, K. Y. Guslienko, and S. K. Kim, Strong Radiation of Spin Waves by Core Reversal of a Magnetic Vortex and their Wave Behaviors in Magnetic Nanowire Waveguides, *Phys. Rev. Lett.* **98**, 087205 (2007).
- [15] M. Mruczkiewicz, P. Gruszecki, M. Krawczyk, and K. Y. Guslienko, Azimuthal spin-wave excitations in magnetic nanodots over the soliton background: Vortex, Bloch, and Néel-like skyrmions, *Phys. Rev. B* **97**, 064418 (2018).
- [16] Z. Li, B. Dong, Y. He, A. Chen, X. Li, J. H. Tian, and C. Yan, Propagation of spin waves in a 2D vortex network, *Nano Lett.* **21**, 4708 (2021).
- [17] S. K. Kim and Y. Tserkovnyak, Chiral Edge Mode in the Coupled Dynamics of Magnetic Solitons in a Honeycomb Lattice, *Phys. Rev. Lett.* **119**, 077204 (2017).

- [18] C. Behncke, M. Hänze, C. F. Adolff, M. Weigand, and G. Meier, Band structure engineering of two-dimensional magnonic vortex crystals, *Phys. Rev. B* **91**, 224417 (2015).
- [19] C. Behncke, C. F. Adolff, N. Lenzing, M. Hänze, B. Schulte, M. Weigand, G. Schütz, and G. Meier, Spin-wave interference in magnetic vortex stacks, *Commun. Phys.* **1**, 50 (2018).
- [20] B. Taurel, T. Valet, V. V. Naletov, N. Vukadinovic, G. de Loubens, and O. Klein, Complete mapping of the spin-wave spectrum in a vortex-state nanodisk, *Phys. Rev. B* **93**, 184427 (2016).
- [21] K. Y. Guslienko, A. N. Slavin, V. Tiberkevich, and S. K. Kim, Dynamic Origin of Azimuthal Modes Splitting in Vortex-State Magnetic Dots, *Phys. Rev. Lett.* **101**, 247203 (2008).
- [22] F. Hoffmann, G. Woltersdorf, K. Perzlmaier, A. N. Slavin, V. S. Tiberkevich, A. Bischof, D. Weiss, and C. H. Back, Mode degeneracy due to vortex core removal in magnetic disks, *Phys. Rev. B* **76**, 014416 (2007).
- [23] K. Y. Guslienko, G. N. Kakazei, J. Ding, X. M. Liu, and A. O. Adeyeye, Giant moving vortex mass in thick magnetic nanodots, *Sci. Rep.* **5**, 13881 (2015).
- [24] M. W. Yoo, J. Lee, and S. K. Kim, Radial-spin-wave-mode-assisted vortex-core magnetization reversals, *Appl. Phys. Lett.* **100**, 172413 (2012).
- [25] M. Kammerer, M. Weigand, M. Curcic, M. Noske, M. Sproll, A. Vansteenkiste, B. Van Waeyenberge, H. Stoll, G. Woltersdorf, C. H. Back *et al.*, Magnetic vortex core reversal by excitation of spin waves, *Nat. Commun.* **2**, 279 (2011).
- [26] Z. Wang, Y. Cao, R. Wang, B. Liu, H. Meng, and P. Yan, Effect of Dzyaloshinskii-Moriya interaction on magnetic vortex switching driven by radial spin waves, *J. Magn. Magn. Mater.* **512**, 167014 (2020).
- [27] H. G. Bauer, M. Sproll, C. H. Back, and G. Woltersdorf, Vortex Core Reversal Due to Spin Wave Interference, *Phys. Rev. Lett.* **112**, 077201 (2014).
- [28] M. Helsen, A. Gangwar, J. De Clercq, A. Vansteenkiste, M. Weigand, C. H. Back, and B. Van Waeyenberge, Non-linear radial spinwave modes in thin magnetic disks, *Appl. Phys. Lett.* **106**, 032405 (2015).
- [29] H. K. Park, J. H. Lee, J. Yang, and S. K. Kim, Interaction of spin waves propagating along narrow domain walls with a magnetic vortex in a thin-film-nanostrip cross-structure, *J. Appl. Phys.* **127**, 183906 (2020).
- [30] J. P. Park and P. A. Crowell, Interactions of Spin Waves with a Magnetic Vortex, *Phys. Rev. Lett.* **95**, 167201 (2005).
- [31] S. M. Seo, H. W. Lee, H. Kohno, and K. J. Lee, Magnetic vortex wall motion driven by spin waves, *Appl. Phys. Lett.* **98**, 012514 (2011).
- [32] J. Han, P. Zhang, J. T. Hou, S. A. Siddiqui, and L. Liu, Mutual control of coherent spin waves and magnetic domain walls in a magnonic device, *Science* **366**, 1121 (2019).
- [33] W. Yu, J. Lan, and J. Xiao, Magnetic Logic Gate Based on Polarized Spin Waves, *Phys. Rev. Appl.* **13**, 024055 (2020).
- [34] M. Buess, R. Höllinger, T. Haug, K. Perzlmaier, U. Krey, D. Pescia, M. R. Scheinfein, D. Weiss, and C. H. Back, Fourier Transform Imaging of Spin Vortex Eigenmodes, *Phys. Rev. Lett.* **93**, 077207 (2004).
- [35] M. Buess, T. Haug, M. R. Scheinfein, and C. H. Back, Micromagnetic Dissipation, Dispersion, and Mode Conversion in Thin Permalloy Platelets, *Phys. Rev. Lett.* **94**, 127205 (2005).
- [36] K. Vogt, O. Sukhostavets, H. Schultheiss, B. Obry, P. Pirro, A. A. Serga, T. Sebastian, J. Gonzalez, K. Y. Guslienko, and B. Hillebrands, Optical detection of vortex spin-wave eigenmodes in microstructured ferromagnetic disks, *Phys. Rev. B* **84**, 174401 (2011).
- [37] X. Zhu, Z. Liu, V. Metlushko, P. Grütter, and M. R. Freeman, Broadband spin dynamics of the magnetic vortex state: Effect of the pulsed field direction, *Phys. Rev. B* **71**, 180408 (2005).
- [38] L. Giovannini, F. Montoncello, F. Nizzoli, G. Gubbiotti, G. Carlotti, T. Okuno, T. Shinjo, and M. Grimsditch, Spin excitations of nanometric cylindrical dots in vortex and saturated magnetic states, *Phys. Rev. B* **70**, 172404 (2004).
- [39] V. Novosad, M. Grimsditch, K. Yu. Guslienko, P. Vavassori, Y. Otani, and S. D. Bader, Spin excitations of magnetic vortices in ferromagnetic nanodots, *Phys. Rev. B* **66**, 052407 (2002).
- [40] J. P. Park, P. Eames, D. M. Engebretson, J. Berezovsky, and P. A. Crowell, Imaging of spin dynamics in closure domain and vortex structures, *Phys. Rev. B* **67**, 020403R (2003).
- [41] B. A. Ivanov and C. E. Zaspel, High Frequency Modes in Vortex-State Nanomagnets, *Phys. Rev. Lett.* **94**, 027205 (2005).
- [42] S. Mayr, L. Flajšman, S. Finizio, A. Hrabec, M. Weigand, J. Förster, H. Stoll, L. J. Heyderman, M. Urbánek, S. Wintz *et al.*, Spin-wave emission from vortex cores under static magnetic bias fields, *Nano Lett.* **21**, 1584 (2021).
- [43] M. Buess, T. P. J. Knowles, R. Höllinger, T. Haug, U. Krey, D. Weiss, D. Pescia, M. R. Scheinfein, and C. H. Back, Excitations with negative dispersion in a spin vortex, *Phys. Rev. B* **71**, 104415 (2005).
- [44] D. Osuna Ruiz, P. S. Keatley, J. R. Childress, J. A. Katine, R. J. Hicken, A. P. Hibbins, and F. Y. Ogrin, Time-domain imaging of curling modes in a confined magnetic vortex and a micromagnetic study exploring the role of spiral spin waves emitted by the core, *Phys. Rev. B* **103**, 064408 (2021).
- [45] Z. Wang, H. Y. Yuan, Y. Cao, and P. Yan, Twisted Magnon Frequency Comb and Penrose Superradiance, *Phys. Rev. Lett.* **129**, 107203 (2022).
- [46] A. Khitun, M. Bao, and K. L. Wang, Magnonic logic circuits, *J. Phys. D: Appl. Phys.* **43**, 264005 (2010).
- [47] J. Lan and J. Xiao, Skew scattering and side jump of spin wave across magnetic texture, *Phys. Rev. B* **103**, 054428 (2021).
- [48] C. Schutte and M. Garst, Magnon-skyrmion scattering in chiral magnets, *Phys. Rev. B* **90**, 094423 (2014).
- [49] L. Landau and E. Lifshitz, On the theory of the dispersion of magnetic permeability in ferromagnetic bodies, *Phys. Z. Sowjet.* **8**, 153 (1935) [*Persp. Theor. Phys.*, **51** (1992)].
- [50] T. L. Gilbert, A phenomenological theory of damping in ferromagnetic materials, *IEEE Trans. Magn.* **40**, 3443 (2004).
- [51] A. Vansteenkiste, J. Leliaert, M. Dvornik, M. Helsen, F. Garcia-Sanchez, and B. Van Waeyenberge, The design and verification of MuMax3, *AIP Advances* **4**, 107133 (2014).
- [52] Z. C. Gao, Y. Su, L. Weng, J. Hu, and C. Park, Quantifying arbitrary-spin-wave-driven domain wall motion, the creep nature of domain wall and the mechanism for domain wall advances, *New J. Phys.* **21**, 063014 (2019).
- [53] Z. C. Gao, Y. Su, B. Xi, J. Hu, and C. Park, The origin of spin wave pulse-induced domain wall inertia, *J. Phys.: Condens. Matter* **32**, 475803 (2020).

- [54] Z. C. Gao, Y. Yang, Y. Su, J. Hu, and C. Park, The interactions between spin wave and stacked domain walls, *J. Phys.: Condens. Matter* **33**, 065806 (2021).
- [55] Z. Wang, Y. Cao, and P. Yan, Goos-Hänchen effect of spin waves at heterochiral interfaces, *Phys. Rev. B* **100**, 064421 (2019).
- [56] P. Gruszecki, Y. S. Dadoenkova, N. N. Dadoenkova, I. L. Lyubchanskii, J. Romero-Vivas, K. Y. Guslienko, and M. Krawczyk, Influence of magnetic surface anisotropy on spin wave reflection from the edge of ferromagnetic film, *Phys. Rev. B* **92**, 054427 (2015).
- [57] A. Mook, B. Gobel, J. Henk, and I. Mertig, Magnon transport in noncollinear spin textures: Anisotropies and topological magnon Hall effects, *Phys. Rev. B* **95**, 020401(R) (2017).
- [58] K. A. van Hoogdalem, Y. Tserkovnyak, and D. Loss, Magnetic texture-induced thermal Hall effects, *Phys. Rev. B* **87**, 024402 (2013).
- [59] M. Mochizuki, X. Z. Yu, S. Seki, N. Kanazawa, W. Koshihara, J. Zang, M. Mostovoy, Y. Tokura, and N. Nagaosa, Thermally driven ratchet motion of a skyrmion microcrystal and topological magnon Hall effect, *Nat. Mater.* **13**, 241 (2014).
- [60] S. E. Barnes and S. Maekawa, Generalization of Faraday's Law to Include Nonconservative Spin Forces, *Phys. Rev. Lett.* **98**, 246601 (2007).
- [61] S. A. Yang, G. S. D. Beach, C. Knutson, D. Xiao, Q. Niu, M. Tsoi, and J. L. Erskine, Universal Electromotive Force Induced by Domain Wall Motion, *Phys. Rev. Lett.* **102**, 067201 (2009).
- [62] N. Nagaosa and Y. Tokura, Topological properties and dynamics of magnetic skyrmions, *Nat. Nanotechnol.* **8**, 899 (2013).
- [63] N. Papanicolaou and T. N. Tomaras, Dynamics of magnetic vortices, *Nucl. Phys. B* **360**, 425 (1991).
- [64] P. Yan, X. S. Wang, and X. R. Wang, All-Magnonic Spin-Transfer Torque and Domain Wall Propagation, *Phys. Rev. Lett.* **107**, 177207 (2011).
- [65] J. Lan, W. Yu, R. Wu, and J. Xiao, Spin-Wave Diode, *Phys. Rev. X* **5**, 041049 (2015).
- [66] H. Yu, J. Xiao, and H. Schultheiss, Magnetic texture based magnonics, *Phys. Rep.* **905**, 1 (2021).
- [67] B. Göbel, I. Mertig, and O. A. Tretiakov, Beyond skyrmions: Review and perspectives of alternative magnetic quasiparticles, *Phys. Rep.* **895**, 1 (2020).
- [68] S. B. Choe, Y. Acremann, A. Scholl, A. Bauer, A. Doran, J. Stöhr, and H. A. Padmore, Vortex core-driven magnetization dynamics, *Science* **304**, 420 (2004).
- [69] A. A. Thiele, Steady-state Motion of Magnetic Domains, *Phys. Rev. Lett.* **30**, 230 (1973).
- [70] K. Yu. Guslienko, B. A. Ivanov, V. Novosad, Y. Otani, H. Shima, and K. Fukamichi, Eigenfrequencies of vortex state excitations in magnetic submicron-size disks, *J. Appl. Phys.* **91**, 8037 (2002).
- [71] K. Yu. Guslienko, X. F. Han, D. J. Keavney, R. Divan, and S. D. Bader, Magnetic Vortex Core Dynamics in Cylindrical Ferromagnetic Dots, *Phys. Rev. Lett.* **96**, 067205 (2006).
- [72] X. G. Wang, G. H. Guo, Y. Z. Nie, G. F. Zhang, and Z. X. Li, Domain wall motion induced by the magnonic spin current, *Phys. Rev. B* **86**, 054445 (2012).
- [73] X. G. Wang, G. H. Guo, G. F. Zhang, Y. Z. Nie, and Q. L. Xia, An analytical approach to the interaction of a propagating spin wave and a Bloch wall, *Appl. Phys. Lett.* **102**, 132401 (2013).
- [74] S. Macke and D. Goll, Transmission and reflection of spin waves in the presence of Néel walls, *J. Phys.: Conf. Ser.* **200**, 042015 (2010).
- [75] J. Kim and S. Choe, Simple harmonic oscillation of ferromagnetic vortex core, *J. Magn.* **12**, 113 (2007).
- [76] K. Y. Guslienko, G. R. Aranda, and J. Gonzalez, Spin torque and critical currents for magnetic vortex nano-oscillator in nanopillars, *J. Phys.: Conf. Ser.* **292**, 012006 (2011).
- [77] B. A. Ivanov and C. E. Zaspel, Excitation of Spin Dynamics by Spin-Polarized Current in Vortex State Magnetic Disks, *Phys. Rev. Lett.* **99**, 247208 (2007).
- [78] J. C. Slonczewski, Current-driven excitation of magnetic multilayers, *J. Magn. Magn. Mater.* **159**, L1 (1996).
- [79] J. C. Slonczewski, Excitation of spin waves by an electric current, *J. Magn. Magn. Mater.* **195**, L261 (1999).
- [80] X. M. Cheng, K. S. Buchanan, R. Divan, K. Y. Guslienko, and D. J. Keavney, Nonlinear vortex dynamics and transient domains in ferromagnetic disks, *Phys. Rev. B* **79**, 172411 (2009).
- [81] K. Y. Guslienko, O. V. Sukhostavets, and D. V. Berkov, Nonlinear magnetic vortex dynamics in a circular nanodot excited by spin-polarized current, *Nanoscale Res. Lett.* **9**, 386 (2014).
- [82] Z. Ren, L. Jin, T. Wen, Y. Liao, X. Tang, H. Zhang, and Z. Zhong, MuFA (Multi-type Fourier Analyzer): A tool for batch generation of MuMax3 input scripts and multi-type Fourier analysis from micromagnetic simulation output data, *Comput. Phys. Commun.* **244**, 311 (2019).
- [83] K. Y. Guslienko, R. W. Chantrell, and A. N. Slavin, Dipolar localization of quantized spin-wave modes in thin rectangular magnetic elements, *Phys. Rev. B* **68**, 024422 (2003).
- [84] J. Jorzick, S. O. Demokritov, B. Hillebrands, M. Bailleul, C. Fermon, K. Y. Guslienko, A. N. Slavin, D. V. Berkov, and N. L. Gorn, Spin Wave Wells in Nonellipsoidal Micrometer Size Magnetic Elements, *Phys. Rev. Lett.* **88**, 047204 (2002).
- [85] R. Hertel, W. Wulfhekel, and J. Kirschner, Domain-wall Induced Phase Shifts in Spin Waves, *Phys. Rev. Lett.* **93**, 257202 (2004).
- [86] C. Bayer, H. Schultheiss, B. Hillebrands, and R. L. Stamps, Phase shift of spin waves traveling through a 180°/spl deg/Bloch-domain wall, *IEEE Trans. Magn.* **41**, 3094 (2005).